IMAGE CONSTRUCTION AND CANCER TISSUE DETECTION ALGORITHMS FOR PORTABLE CONFOCAL MICROSCOPY SYSTEM

by

Gamze Koç

B.S., Electrical Electronics Engineering, Middle East Technical University, 2011

Submitted to the Institute for Graduate Studies in
Science and Engineering in partial fulfillment of
the requirements for the degree of
Master of Science

Graduate Program in Electrical and Electronics Engineering
Boğaziçi University
2014

IMAGE CONSTRUCTION AND CANCER TISSUE DETECTION ALGORITHMS FOR PORTABLE CONFOCAL MICROSCOPY SYSTEM

APPROVED BY:

Assist. Prof. İsmail Faik Başkaya (Thesis Supervisor)	.....
Assist. Prof. Baykal Sarıoğlu (Thesis Co-supervisor)	.....
Prof. Emin Anarım	.....
Assoc. Prof. Burak Acar	.....
Assist. Prof. Yiğit Dağhan Gökdel	.....

DATE OF APPROVAL: 22.07.2014

ACKNOWLEDGEMENTS

First of all, I thank my thesis advisor Assist. Prof. Faik Başkaya. He honored me by accepting me as a master student under his supervision.

I would like to thank to Assist. Prof. Baykal Sarıoğlu for his patience when he listens my ideas, deals with my problems all the time and his amazing guidance which always helped me to extend my viewpoint.

I thank Assist. Prof. Yiğit Dağhan Gökdel for his great recommendations which make a major contribution to my thesis.

I thank my jury comitee members Prof. Emin Anarım and Assoc. Prof. Burak Acar for their incentive recommendations at my thesis defense.

Lastly, I have my special appreciation to the most important person in my life, my father Yaşar Koç for his confidence on my choices and his endless love and support. As a teacher, he always supports me to continue my education as far as I can get far.

ABSTRACT

IMAGE CONSTRUCTION AND CANCER TISSUE DETECTION ALGORITHMS FOR PORTABLE CONFOCAL MICROSCOPY SYSTEM

This thesis focuses on three main issues; namely, (i) image acquisition of cancer tissue, (ii) image stitching and (iii) image processing for cancer detection. An algorithm and a related circuity are implemented to create images from signals obtained by a photomultiplier tube (PMT) for the image acquisition part. Data acquisition card and MATLAB are used to acquire signals and create images. The current generated by photomultiplier tube, coming signal is converted to a voltage signal by the designed circuit. Afterwards, implemented algorithm transforms this voltage to a meaningful image and then displays on the screen. The second issue is image stitching. Image stitching is a method which combines a sequence of partially overlapping images into a merged image using an appropriate transformation. Generally, in image stitching, features of images are detected, described and stored to find matching points. Next, two images are combined with respect to the similarity of matching points in the light of implemented transformation. Image stitching algorithms in the literature are investigated. Final section composes of image processing for cancer detection. Two different kinds of novel classifiers are developed to detect cancer. The first one depends on the analysis of root mean square error (RMSE) owing to line plot of center row of images in the Fourier domain. Unlike healthy tissue, cancerous tissue has an irregular structure because of uncontrollable growth in the cells. Hence, it has been noticed that line plot of the center row has even, symmetric function characteristic if it is healthy tissue image. The other classifier depends on histogram-based threshold technique. It has been realized that cancerous tissue images have darker pixel values than healthy tissue images. Therefore, histogram is considered as a tool to detect cancer.

ÖZET

TAŞINABİLİR KONFOKAL MİKROSKOP SİSTEMİ İÇİN GÖRÜNTÜ ÜRETİLMESİ VE KANSERLİ DOKU TESPİTİ ALGORİTMALARI

Bu tez üç ana konu üzerine odaklanmıştır. Bunlar (i) kanserli dokudan görüntü elde edilmesi, (ii) görüntü birleştirme ve (iii) kanser tespiti için görüntü işlemedir. İmge elde etme kısmında, bir fotomultiplikatör tarafından elde edilen işaretlerden görüntü yaratmak için bir algoritma ve bir devre geliştirilmiştir. Veri toplama kartı ve MATLAB, işaretleri elde etmek ve görüntü yaratmak için kullanılmıştır. Fotomultiplikatör tarafından üretilen akım işareti, tasarlanan devre ile gerilime dönüştürülmüştür. Sonrasında, geliştirilen algoritma, bu gerilim işaretini anlamlı bir imgeye çevirmiş ve ekranda göstermiştir. İkinci konu ise görüntü birleştirmedir. İmge birleştirmede kısmi çakışmaları olan bir grup görüntü, uygun dönüşüm kullanılarak tek bir kaynaşmış görüntüye dönüştürülür. Bu aşamada, görüntülerin öznitelikleri tespit edilir, tanımlanır ve uygun noktaları bulmak için saklanır. Daha sonra, iki görüntü, geliştirilen dönüşüm kullanılarak uyuşan noktalara göre birleştirilir. Literatürdeki imge birleştirme algoritmaları araştırılmıştır. Son kısım, kanser tespiti için görüntü işlemeden oluşmaktadır. Kanseri tespit etmek için iki yeni sınıflandırıcı geliştirilmiştir. İlki, Fourier tanım kümesindeki görüntünün merkezindeki satırın grafiğinin etkin değer hatasının incelenmesine dayanmaktadır. Kanserli doku, hücrelerdeki kontrol edilemeyen büyümeden ötürü düzensiz bir yapıya sahiptir. Bu nedenle, eğer imge sağlıklı dokuya aitse, imgenin merkezdeki satırın grafiğinin çift, simetrik bir fonksiyon karakteristiğine sahip olduğu fark edilmiştir. Diğer sınıflandırıcı histograma bağlı eşik değer tekniğine dayanmaktadır. Sağlıklı dokudan farklı olarak, kanserli doku imgelerinde, sağlıklı doku imgelerinden daha fazla koyu renk piksel olduğu fark edilmiştir. Bundan ötürü, histogram, kanser tespitinde araç olarak kullanılmıştır.

TABLE OF CONTENTS

LIST OF FIGURES

LIST OF TABLES

LIST OF SYMBOLS

C	The current amplification
C_1, C_2	Variables to balance the division with weak denominator
D	Total number of dynodes
$D(x, y, \sigma)$	Difference of Gaussian image
$f(m, n)$	2D representation of point
f(x,y)	Signal representation function of 2D space defined over an x-y plane
$F(j, k)$	Original image
$\bar{F}(j, k)$	Distorted image
$F(u, v)$	2D spectrum of $f(x, y)$
g_i	Set of gray levels
g_n	The gain of the n^{th} dynode
$G(x, y, \sigma)$	Gaussian blurring function
$h(g_i)$	The height of the histogram at gray levels
H	Homography matrix
i	The number of gray levels in the image
$I(x, y)$	Input image
L	Dynamic range of the pixel-values
$L(x, y, \sigma)$	Blurred image
$m(x, y)$	Gradient magnitude
n	Total number of pixels
n_a	The number of electrons collected
n_{dark}	Percentage of dark pixels
n_k	The number of photoelectrons which strike the first dynode
n_{light}	Percentage of light pixels
M	Iterations of the minimum count of points represented as m
p	The possibility that at least one of the sets of random samples have inliers
Q	Universal image quality index

t	Threshold
u	The possibility that any certain data point is an inlier
v	The probability of having outlier
w	Spatial frequency x direction
x_i	Value of the pixel
$x_i^{'}$	Reciprocal pixel value
x_1	Position of a pixel in original image
x_2	Position of a pixel in the merged image
x_k, y_k, w_k	Keypoint positions
y_i	The number of pixels in the image with gray level i
z	Spatial frequency in y direction
σ_{xy}	Covariance of x and y
μ_x	Mean of x
μ_y	Mean of y
$\theta(x, y)$	Orientation
σ_x^2	Variance of x
σ_y^2	Variance of y

LIST OF ACRONYMS/ABBREVIATIONS

2D	Two Dimensional
3D	Three Dimensional
AUROC	Area Under Receiver Operating Characteristic
CIN	Cervical Intraepithelial Neoplasia
CT	Computerized Tomography
DAQ	Data Acquisition
FFT	Fast Fourier Transform
FN	False Negative
FP	False Positive
FSIM	Feature Similarity Index
GMM	Gaussian Mixture Modal
GLOH	Gradient Location and Orientation Histogram
LSCM	Laser Scanning Confocal Microscopy
MRI	Magnetic Resonance Imaging
MEMS	Micro-electromechanical Systems
N	Iteration Number
PC	Phase Congruency
PAC-SIFT	Principal Components Analysis - Scale invariant Feature Transform
RANSAC	Random Sample Consensus
ROC	Receiver Operating Characteristic
RMSE	Root Mean Square Error
SIFT	Scale-invariant Feature Transform
SSIM	Structural Similarity Measurement Index
SVM	Support Vector Machine
TN	True Negative
TP	True Positive
UQI	Universal Quality Index

1. INTRODUCTION

Cancer disease is known as one of the deadliest and most dangerous health problems. All over the world, approximately six million people die because of cancer every year; in addition, more than ten million people get cancer [1]. Overall morality rate of cancer (particularly trachea, lung, colon, rectal, chest and stomach cancer) is more than 13% especially in the middle/high income countries such as Turkey [2]. Moreover, 85% of cancer cases occur in epithelial tissue and form the most deadly types such as lung, stomach, skin, colon, uterus and bladder [3].

Cancer is a process which starts by building blocks. Normal cells get segmentation when the body needs it and they die when they get old. Therefore, new cells replace with older ones. However, sometimes, this process breaks down. New cells are produced although the body does not need them and older cells do not die. These newly produced cells become integrated and create cysts and tumours [4]. Therefore, one cell has more than one cell nuclei in cancerous tissues and the density of the tissue becomes irregular. Accordingly, it becomes much more difficult to analyse cancerous images and diagnosis which depends on only human eye couldn't give absolute results [5].

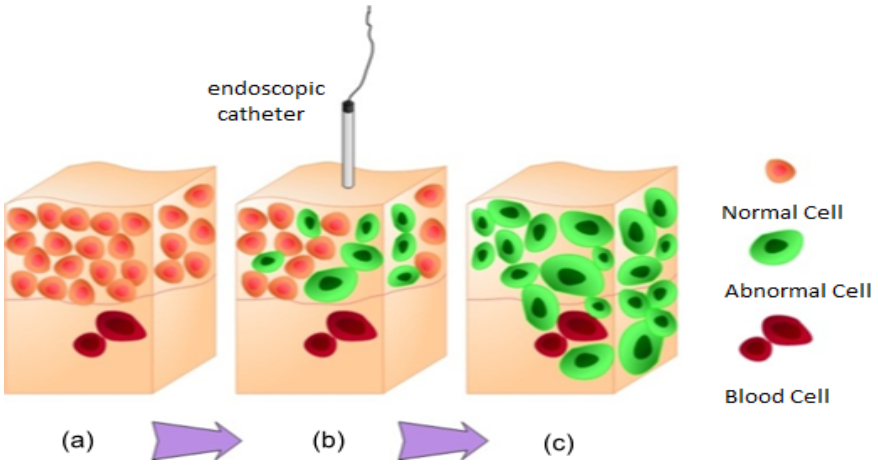

Figure 1.1. Structure of Stratified Squamous Epithelium Tissue (a) Normal case (b) Dysplastic case (c) Metastatic case [6].

Stratified squamous epithelium tissue can be seen in Figure 1.1. It has three layers which are surface layer, basal membrane and connective tissue at base. Neoplastic cells, i.e. cancerous cells, start existing throughout basal membrane, then cover the whole epithelium tissue by increasing upward. They pass through basal membrane and reach to connective tissue as shown in Figure 1.1 in part c. Additionally, one normal and one cancerous epithelium cells are depicted in Figure 1.2.

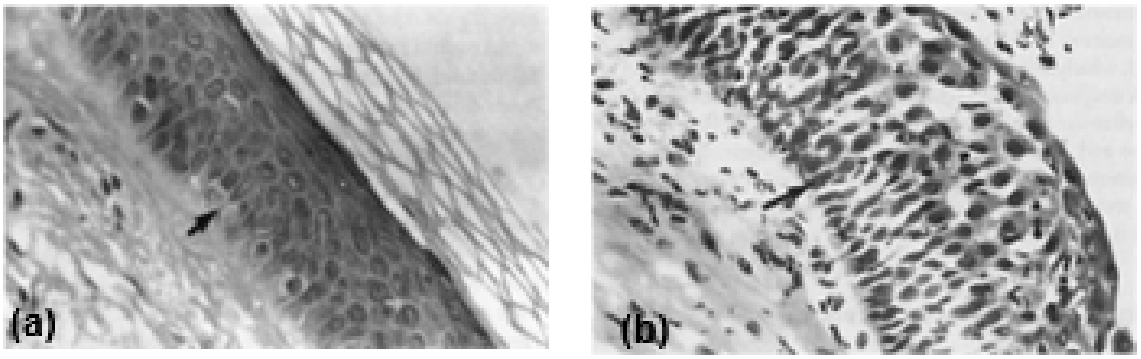

Figure 1.2. (a) Normal Epithelium Cell (b) Cancerous Epithelium Cell [7].

1.1. Cancer Detection Methods and Their Comparisons

Due to reasons which were mentioned before, medical image processing in cancer detection is an intensely studied topic. Although it is a very dangerous disease, early diagnosis provides an advantage for treatment [3]. There are several methods used in early diagnosis of cancer. Magnetic Resonance Imaging(MRI), Computerized Tomography(CT) and invasive needle biopsy are common methods among all. However, these methods have several disadvantages. First of all, cancerous tumour should be big enough to be detected. Moreover, CT exposes radiation to the patient and it cannot be frequently used for the same patient due to cancer triggering effect of the radiation [8]. Additionally, since CT and MRI are both expensive imaging technologies, limited number of patients can make use of them.

Another frequently used method is invasive biopsy that uses biopsy catheter in order to get a cell sample from the tissue which was suspected to be cancerous. Biopsy catheter is a device which can be put in human body for treatment or practising

surgical operations. Afterwards, cancer is diagnosed with microscopic examination of the acquired cell sample. However, it has been shown that tumourigenesis can be seen again along the way of the biopsy needle [9].

1.2. Laser Scanning Confocal Microscopy

Cheaper, economic, preferably portable and radiation-less imaging and diagnosis methods are needed in cancer detection because of the aforementioned reasons. Confocal endo-microscopy can be stated as suitable method since it can achieve real-time in-vivo imaging of neoplastic lesions. Laser Scanning Confocal Microscopy(LSCM) scans the sample point-to-point and combines the pixel values to create image. It provides high resolution images with high contrast and does optical sectioning of few hundred micrometers under the tissue. Thus, it enables delicate cancer diagnosis of tumour [10–12].

In general, biopsy based clinical cancer diagnosis method comprises of lots of serial steps as follows tissue freezing, sectioning, paraffinning, histological painting and microscopic examination in the laboratory [13, 14]. Early and accurate diagnosis is essential in order to increase survival rate [15]. Early diagnosis and real-time in-vivo clinical examination are preferred since they reduce cost of operation and wrong diagnosis rate [16].

Deadly epithelial cancer types arise from dysplastic lesions which primarily form in epithelium tissue. These tissue samples are abnormal developments in pathology. At this point, confocal endo-microscopy is frequently preferred because it can detect neoplastic lesions in real time. It is shown that LSCM can achieve giving information about both cell morphology and the structure of the tissue in epithelium. Confocal microscopy has the capacity of tissue visualization like histological examination without tissue extraction by the help of their in-vivo optical sectioning imaging. When the situation needs the intracellular resolution imaging, LSCM can accomplish it with the addition of optically active, molecular directed diagnostic contrast materials. The main aim is to design and implement a cheap, multi-functional and new class device

which can help the early diagnosis of skin, uterus, lung, colon and stomach cancer types. The advantage of implementation of smaller, portable scanning lasers is that they use MEMS as laser scanning device instead of expensive, big, sizeable and traditional galvanometers [17–20]. MEMS scanners are generally used in visualization and screen application areas in order to create a scanning image by reflecting the light beams that came upon them [21–23]. There are various MEMS based micro scanners which utilize different actuation mechanisms in the literature [24]. Silicon(Si) based micro scanners are used in almost all of the hand-held confocal microscope applications [17, 19, 25]. Moreover, stainless steel micro scanner was produced by researchers and used in desktop confocal fluorescence microscope applications [26].

Catheters in in-vivo imaging is a commonly employed technique, especially in ultrasonic imaging applications [27–29]. Thanks to recent developments, catheters are started to be used not only in intravenous applications but also in intra cardiac and natural orifice transluminal endoscopic surgeries [30, 31]. Improvements in confocal catheter microscope technology makes even pretty complex application areas possible.

Cheap and lightweight LSCM is essential to overcome aforementioned disadvantages of traditional cancer diagnosis methods. Therefore, the system in Figure 1.3 offers an innovative approach since it is cheaper, portable and radiationless compared to equivalent methods. In this system, a minimal invasive miniature microscope is integrated with a 7Fr catheter. It is capable of performing in-vivo imaging.

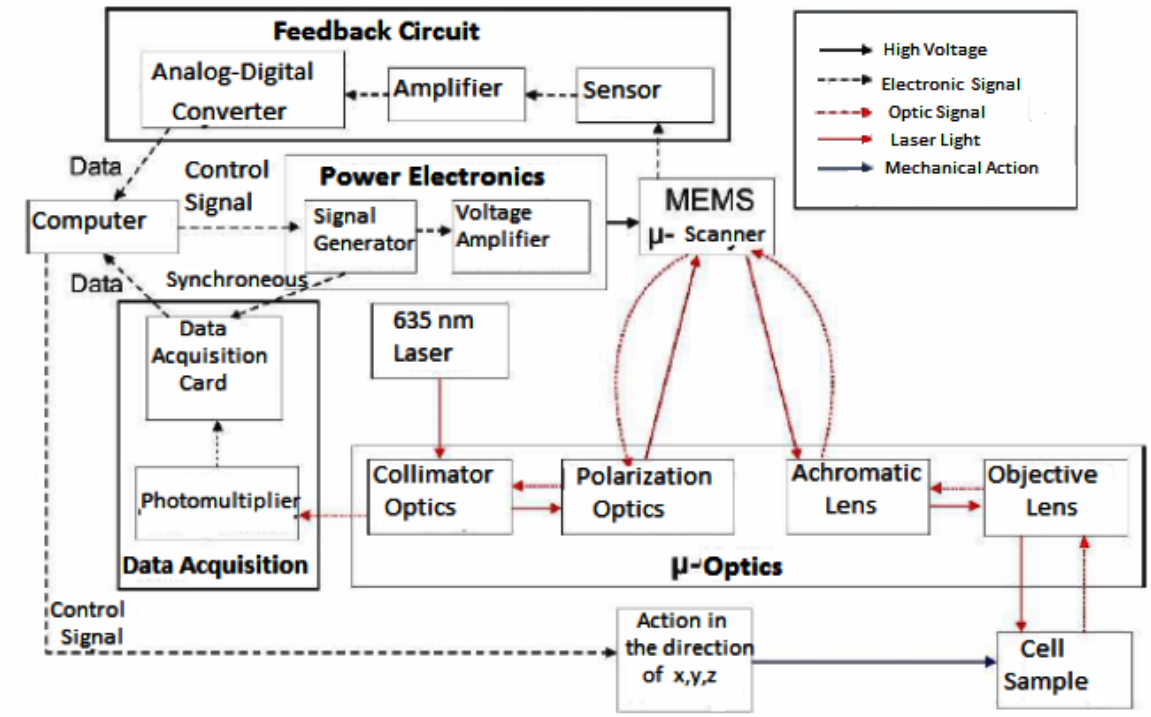

Figure 1.3. Targeted System Diagram [6].

1.3. Operation Principle

Targeted system shown in Figure 1.3 has six parts which are (i) biopsy catheter (ii) MEMS-scanner (iii) miniature micro-opto-mechanical microscope systems (iv) feedback circuit (v) data acquisition and control software (vi) power electronics/driver circuit. The thesis focuses on data acquisition part.

Briefly, 7Fr biopsy catheter which is suitable for micro-electro-mechanical structures is designed and produced firstly to be used in LSCM which includes MEMS based medical technologies. Miniature confocal microscope mechanism, whose diagram is shown below in Figure 1.4, is realized on an optical table in the laboratory by using sensitive micro-electro-mechanical components and devices. Instead of conventional and bulky galvanometers, MEMS based biaxial micro-scanner is placed in the heart of the miniature confocal microscope. A magnetic actuation system is employed.

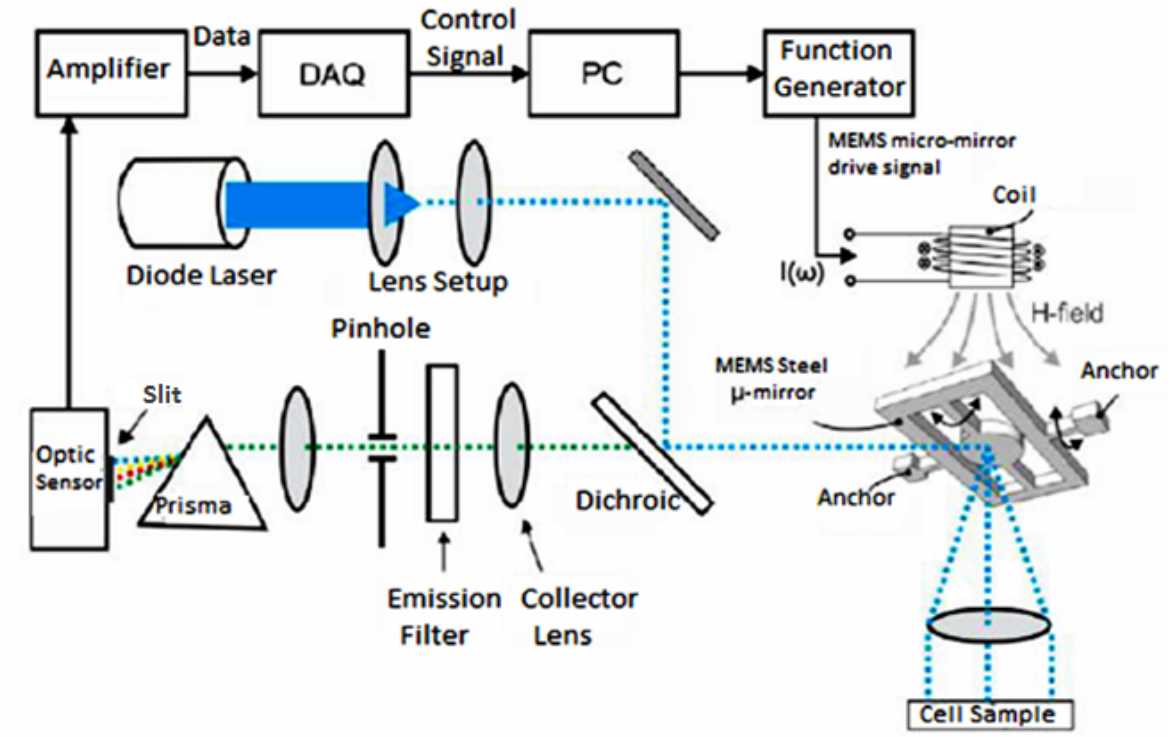

Figure 1.4. Diagram of Confocal Microscope's Optical Architecture [6].

Micro-scanner is controlled with computer by the help of an electronic feedback and a driver circuit. It is crucial to get the position data of micro scanner. In other words, detection of exact position of laser beam on the target cell and driving the scanner accordingly is important to get a correct image. Real time scanning angles for every axis, especially at times when the displacement is large, are detected by the help of the designed feedback system. For this, a compact infra-red detection method which is depicted in Figure 1.5 is used.

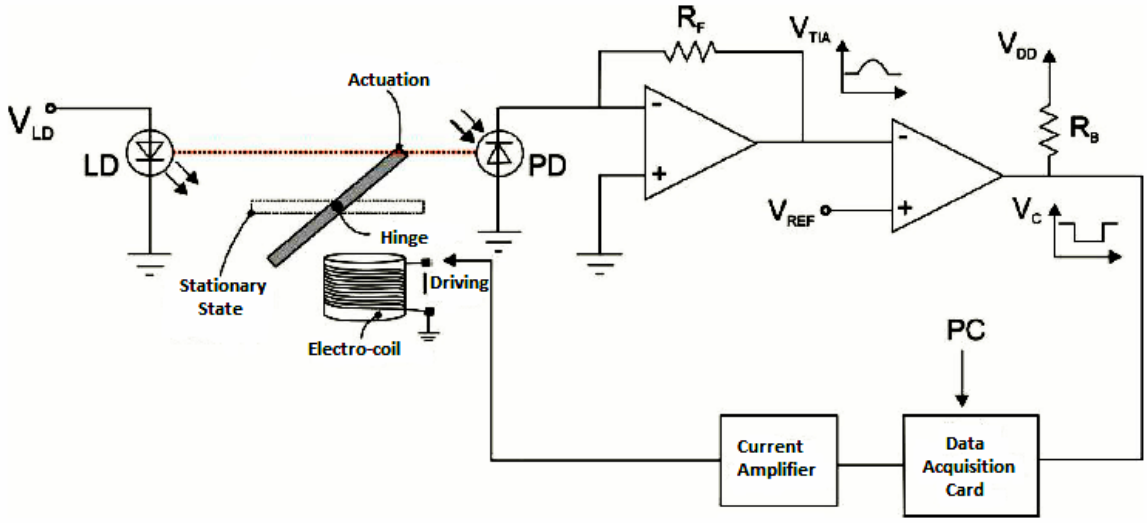

Figure 1.5. Proposed Position Detection System [6].

Magnetic micro scanner is actuated by a miniature electro-coil and electric current. Electric current is produced by data acquisition card under computer control. In order to get the correct image and transfer it to the computer, slow scanning motion of the scanner should be observed. The diagram of position detection system shown in the Figure 1.5. It contains one infra-red diode, one infra-red photo diode, one transimpedance amplifier and a comparator. Infra-red photo diode is aligned to the laser diode. Transimpedance amplifier amplifies the current occurred on photo diode. Finally, Comparator first digitalizes the signal and then send it to the DAQ card.

Optical components are aligned in such a way that the photo diode does not receive any light while micro scanner is fixed. When micro structure starts to move, photo diode starts to collect light; hence, an electronic current is observed.

The voltage value at the output of the transimpedance amplifier is directly proportional with the movement of the MEMS structure. The optical system is aligned such that the output of the amplifier gives the largest voltage when the movement in the slow-scan axis is at the edge. Therefore, every cycle of the micro scanner generates a signal at the output of the comparator circuit, which is related to synchronization impulse. In this way, the initial point of the scan movement can be exactly found.

Afterwards, the DAQ card creates a driving current for the micro scanner thanks to the detected synchronization impulse at the start. Driving current passes through a current amplifier, and then is transmitted to the electro-coil in order to be able to drive the micro scanner in the slow-scan axis. Finally, the whole system is controlled by using one computer through a data acquisition card.

1.4. Outline and Motivation of The Thesis

This thesis focuses on three main issues. The first issue is implementing the image acquisition part in the Figure 1.3. Second issue comprises of the acquired images. The third issue is to implement classifiers whether the obtained images are cancerous or not. Detailed explanation about these three issues are given in the next chapters.

This thesis is organized as follows. In Chapter 2, image construction part is explained. Chapter 3 gives details on image stitching method and used algorithm steps. In Chapter 4, implemented cancer detection algorithms and their respective performance are evaluated. Finally, Chapter 5 concludes with opinions and directions for the future works.

2. IMAGE ACQUISITION

Data acquisition (DAQ) process converts an analog signal to a digital signal. Therefore, real world physical measures can be gathered as digital numerical values. DAQ systems perform the process and produce digital values for computers [32]. They have mainly three parts. The first part is sensing the physical conditions. Sensors change physical conditions to electric signals. The second part is signal conditioning circuitry which prepares electric signals for analog-to-digital conversion. The third part is converting electric signals to digital values by using analog-to-digital converters. In this thesis, PMT is used as sensor. The second and third parts are performed by the DAQ card.

PMT is a light sensitive detector which offers internal high gain. PMTs are very useful for applications include low light intensity. PMT has five main parts which are a photocathode, dynodes, an anode, an external power supply and an external current meter shown in Figure 2.1.

Light passes through a glass or quartz window and then reaches to photocathode. Photocathode is a photo emissive surface. When a photon strikes to the photocathode with adequate energy level, an electron is released. This is called as photoelectric effect. Next, the electron hits the dynodes. Dynodes are an array of electrodes between the cathode and the anode within the PMT. They are used in order to accelerate the electrons. Each dynode holds more positive voltage than the previous one. Therefore, each dynode creates a more powerful pulling force on the electrons. External power supply causes an electric field between the dynodes, the anode and the cathode. The electric field gives kinetic energy to electrons. Hence, more electrons are emitted after each dynode and the electrons acquire much higher energy level after each emission. This process continues until the electrons reach to the anode. The anode collects emitted electrons. Although one electron is emitted at the beginning of the process, lots of electrons are captured at the end of the process. External current meter quantifies the number of gathered electrons at the anode.

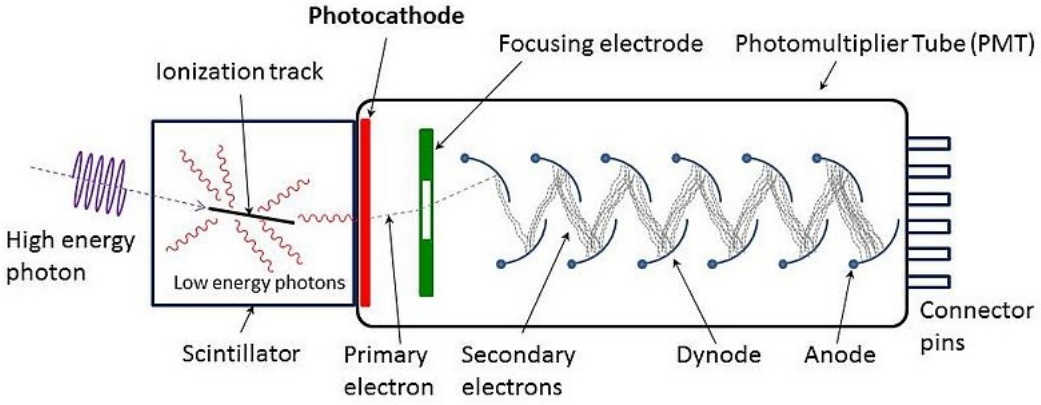

Figure 2.1. Diagram of Photomultiplier Tube's Architecture [33].

Produced current by PMT depends on two factors; the number of electrons are gathered and the gain of the photomultiplier tube. According to [34],

$$n_a = n_k \prod_{n=1}^{D} g_n \tag{2.1}$$

$$C = \frac{n_a}{n_k} \tag{2.2}$$

where

n_k the number of photoelectrons which strike the first dynode,

g_n the gain of the n^{th} dynode,

n_a the number of electrons collected,

D total number of dynodes,

C the current amplification.

In this thesis, H10720 Series photo multiplier tube is used. It can be seen in Figure 2.2. Its maximum output signal current is equal to 100 microampere when 1

volts control voltage is applied. Recommended control voltage adjustment range is between 0.5 volts and 1.1 volts and recommended input voltage range is between 4.5 and 5.5 volts. It has five output cables with different colors; namely, red, black, coaxial black, blue and white as shown in Figure 2.2. Red cable is connected to 5 volts, black cable is connected to ground, white cable is connected to 0.5 volts and black coaxial cable is connected to DAQ card.

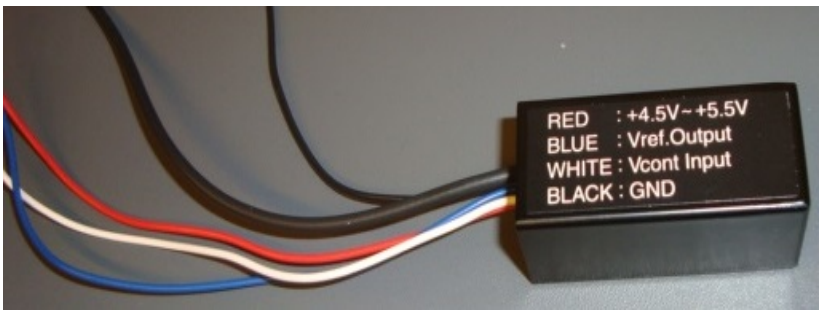

Figure 2.2. H10720 Series Photo Multiplier Tube.

In the first part of the thesis, the PMT collects the increasing light beam and converts it to current. The current is then converted to voltage by implementing the circuit shown in Figure 2.3. UA741CN operational amplifier and 2.2 kohm resistor are used in the circuitry. The implemented circuit can be seen in Figure 2.4.

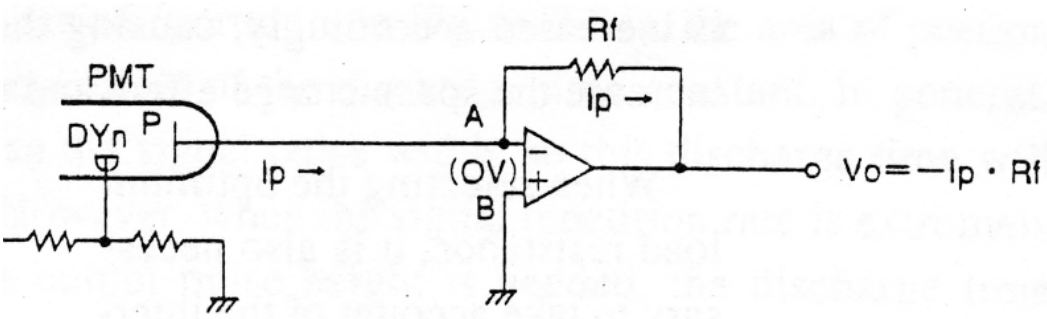

Figure 2.3. Schematic of Current-to-Voltage Converter Circuit [35].

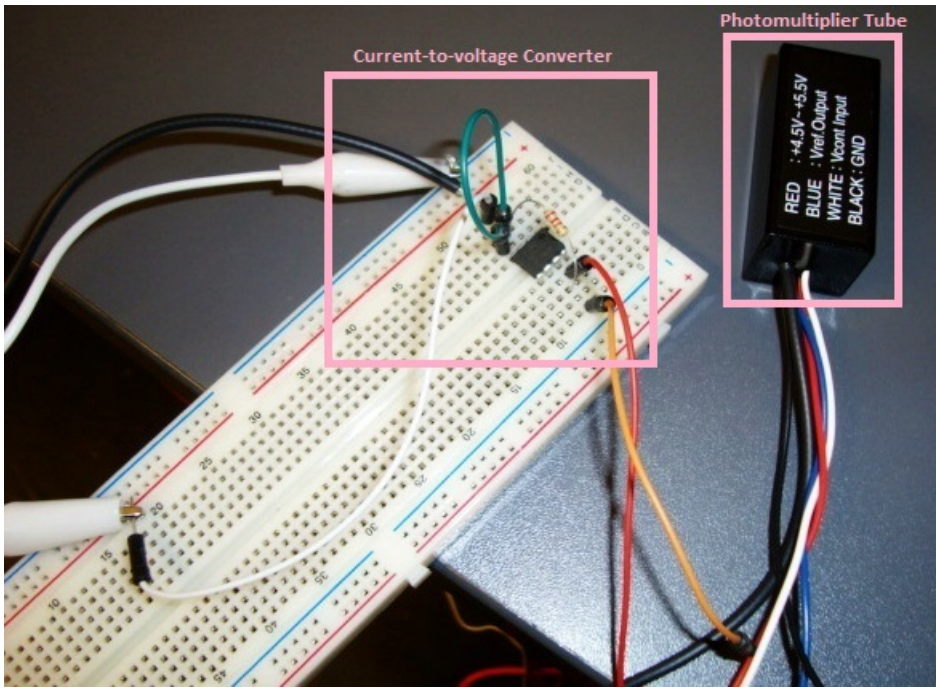

Figure 2.4. Current-to-voltage Converter Circuit.

The voltage taken from the circuit is sent to a computer over DAQ card and processed at MATLAB with the developed algorithm. DAQ card has eight simultaneous analog inputs at 1.25 MS/s/ch with 16-bit resolution, two analog outputs at 3.33 MS/s with 16-bit resolution and 24 digital input/output lines. Experimental set up can be seen in Figure 2.5 and 2.6.

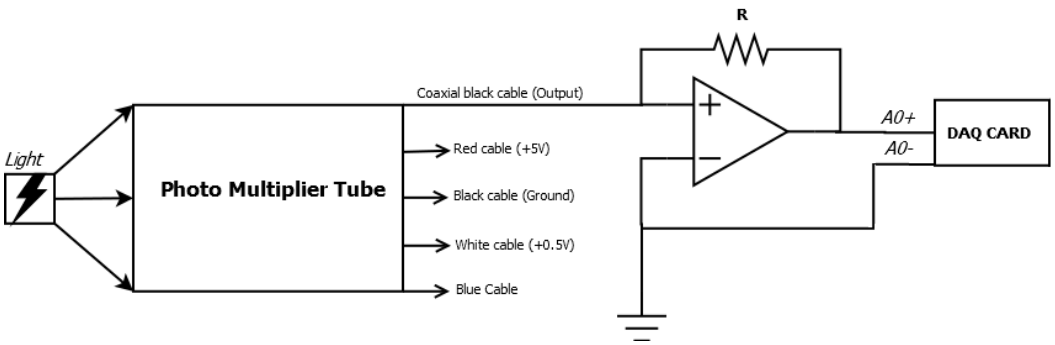

Figure 2.5. System Diagram of Image Acquisition.

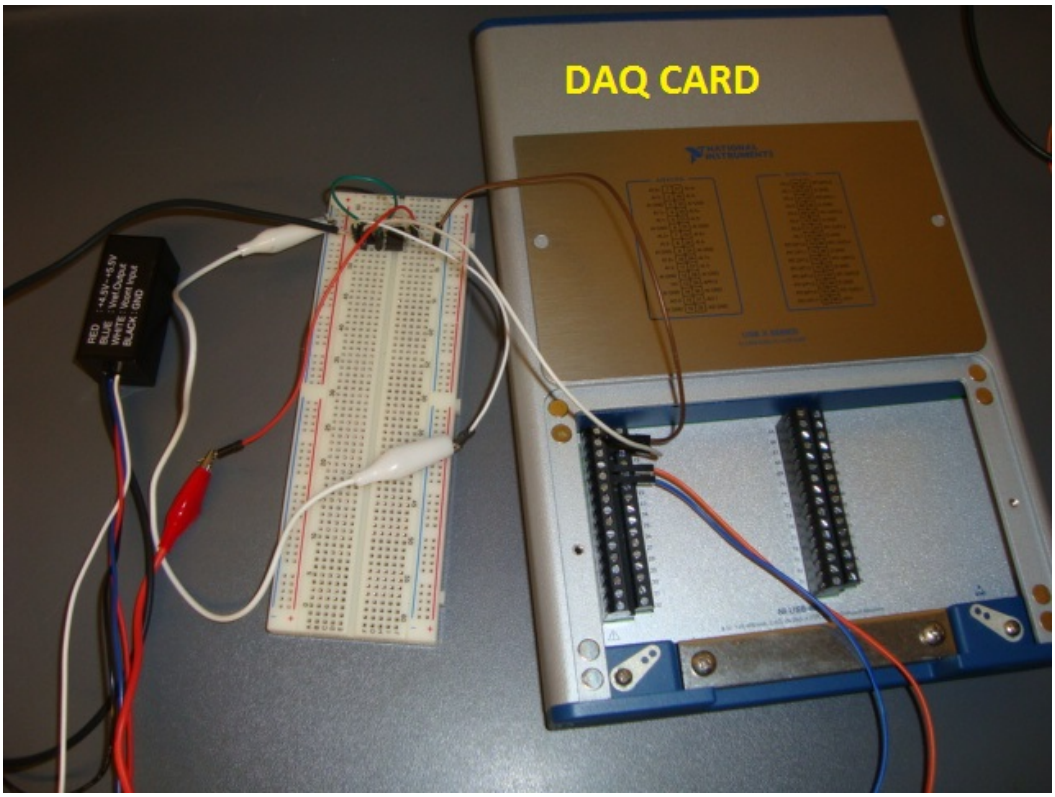

Figure 2.6. Developed Image Data Acquisition System.

The amount of laser beam that is reflected from the tissue is proportional to the tissue density. Dark tissue part reflects laser light beam less than light tissue part. To test the developed system, an obstacle was placed between the photomultiplier tube and light source at certain intervals. Moreover, an algorithm was developed in MATLAB to align pixels correctly. As a result, image in Figure 2.7 is acquired. In the figure, pixels are dark when an obstacle is localized in front of the photomultiplier tube since light intensity is zero. Conversely, pixels are white when there is no obstacle since light intensity is maximum. The reason of this can be explained as follow. Typically, pixel values are in a range of values from 0 to 255 for grayscale images. Black pixel is represented with zero value and white pixel is represented with maximum value. Other values in the range represent different color tones of gray. In conclusion, there are pixels with different color tones of gray in Figure 2.7. They represents different light intensity levels. These levels are formed during removing the obstacle.

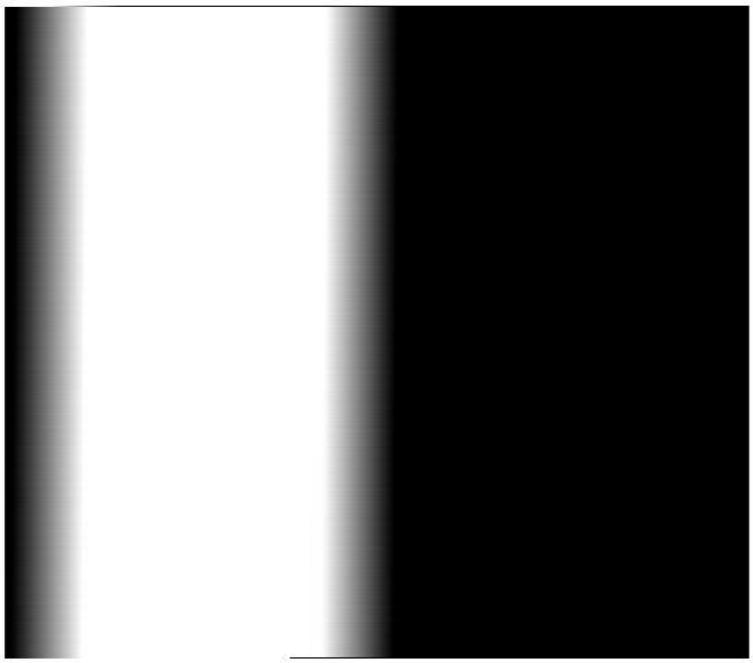

Figure 2.7. Image Acquisition Test Result.

3. IMAGE STITCHING

Confocal microscope cannot acquire whole image of the tissue with one scanning. It can only acquire one part of the image. Therefore, it is essential to stitch partially overlapped images in order to observe whole image. The main goal of image stitching is first getting images which belong to same scene, and then merging them in order to visualize bigger perspective of the scene.

Image alignment is a part of image stitching. Image alignment algorithms find similarity between images within different degrees of overlap. Traditionally, there exists two kinds of automatic image matching algorithms which are direct methods and feature based methods [36]. However, before applying one of these methods, one should choose motion model. Motion models create mathematical relations to point out pixel locations from one image to another. There are several types of motion models such as affine, perspective, rotation, scale, translation, projective etc. After choosing an appropriate motion model, parameters of the model should be estimated. Then, image alignment algorithm is chosen. In direct methods, the main goal is to evaluate camera parameters iteratively by decreasing the error function depending upon intensity change in the region of intersection. The benefit of these methods is that they obtain very accurate registration with respect to the usage of all existing data; however, they rely on the delicate 'brightness constancy' statement which accepts that the intensity of all the pixels of region stays constant between two following images. In feature based methods, correspondences between points or in other words local features, lines or other geometrical entities are determined [36].

In this section of the thesis, previously improved code is used [37]. Flow chart of the algorithm can be seen in Figure 3.1. Methods are used in algorithm are highly suggested in the literature [38–40]. Results can be seen in Table 3.1. Mainly, the whole process has two major parts; feature matching and image matching. In feature matching part, Scale-invariant Feature Transform (SIFT) features of each image are extracted and then matching keypoints are determined between images by the help

of extracted features. In image matching part, homography is calculated with respect to Random Sample Consensus (RANSAC) and then images are stitched in terms of calculated homography.

SIFT was proposed by Lowe in 1999 [41]. It identifies and defines local features in an image. According to [38], SIFT is the best local descriptor. Results of this study prove that SIFT and similar approach Gradient Location and Orientation Histogram (GLOH) features offer the maximum accuracy. SIFT has more tolerance range comparison with the other descriptor due to scalar alteration in the range 2 - 2.5 and rotation alteration in the range 30 – 45 degrees. Blurring affects the SIFT, GLOH and Principal Components Analysis - Scale invariant Feature Transform (PAC-SIFT) less than the other descriptors. Hence, study indicates that SIFT-based descriptors are the most robust descriptors in feature matching. Another important property of SIFT is that it is invariant to rotation, translation, scaling and variations in illumination [42]. Furthermore, it matches features with high probability [43]. It is stable, distinctive and detects local points with high information [44]. Google Scholar statistics proved that SIFT algorithm has been cited in more than 12000 articles [44].

RANSAC was proposed by Fishler and Bolles in 1981 [45]. According to [39], first advantage of RANSAC is that it evaluates all sorts of parameters for any kind of estimation modal. Secondly, it uses the data directly and iteratively estimates parameters using minimal randomly selected sample sets without any assumption. At this point, benefit of RANSAC is using minimum amount of data unlike the others optimization algorithms. According to [40], RANSAC is the most popular robust estimation algorithm in terms of its high tolerance to outliers. Outliers are points which are incoherent with the model. RANSAC estimates the parameters of a modal by using the data consists of many outliers. In addition, Choi *et al.* mentioned another estimators were proposed before RANSAC such as M-estimator or Hough transform. RANSAC uses uncomplicated optimization unlike M-estimator and needs a little amount of memory unlike Hough transform. Finally, homography is estimated with respect to RANSAC and images are stitched using associated homography estimation.

3.1. Scale-invariant Feature Transform

Both direct and feature based methods are not invariant to scale, rotation or brightness variation. Using SIFT algorithm is an appropriate choice, since it is invariant to these variations [46]. Features are extracted from images by using SIFT are well found in both spacial and frequency domain. This protects them from the effect of noise. In addition, features are extracted from a cascaded filtering system in order to reduce cost [41]. Major steps of the SIFT algorithm are explained in the next sections.

3.1.1. Scale-Space Extremum Detection

One can identify positions that are invariant to scale variation of the image by looking for stable features through all potential scales, using a continuous function of scale; in other words, identified as scale space [47]. Scale space of an image is represented as the convolution of variable-scale Gaussian and input image [41];

$$L(x, y, \sigma) = G(x, y, \sigma) * I(x, y) \tag{3.1}$$

where
$L(x, y, \sigma)$ is blurred image,
$G(x, y, \sigma)$ is Gaussian blurring function,
$I(x, y)$ is input image.

$$G(x, y, \sigma) = 1/(2\pi\sigma^2)e^{-(x^2+y^2)/2\sigma^2} \tag{3.2}$$

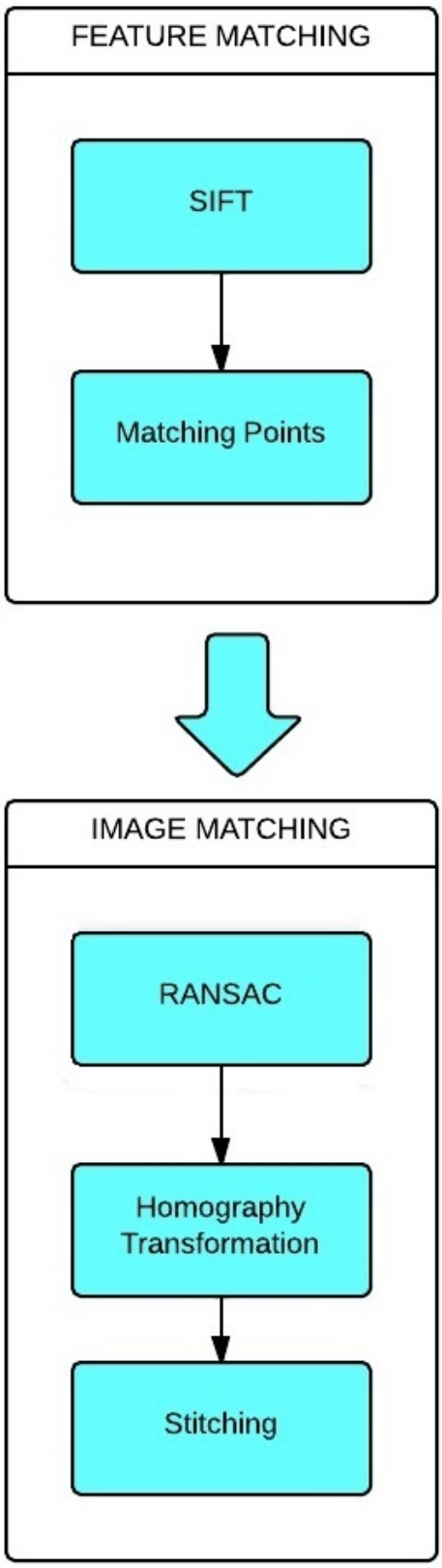

Figure 3.1. Image Stitching Flow Chart.

Difference-of-Gaussian function is calculated to find stable keypoints;

$$D(x, y, \sigma) = (G(x, y, k\sigma) - G(x, y, \sigma)) * I(x, y) = L(x, y, k\sigma) - L(x, y, \sigma) \quad (3.3)$$

$D(x, y, \sigma)$ is the final image which is gathered with the subtraction of two neighbour levels which is divided by a constant k. Representation of equation 3.3 can be seen in Figure 3.2 from [41];

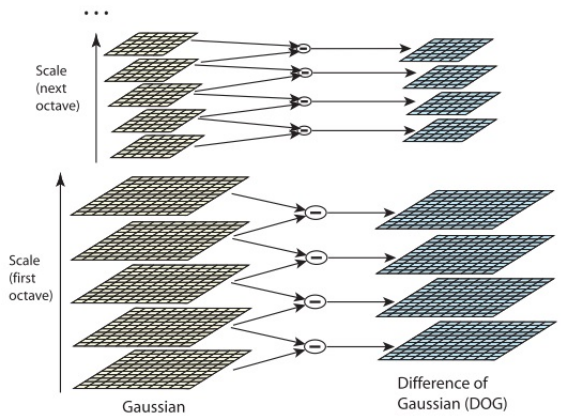

Figure 3.2. Difference-of-Gaussian Images [41].

Finally, local maximum and minimum in the Gaussian pyramid's levels should be found in order to locate keypoints. This can be performed by comparing each pixel with its eight neighbours and nine pixels at above and below of it [46]. This operation can be seen in Figure 3.3. If the pixel passes this test, then it is marked as candidate keypoint.

3.1.2. Keypoint Localization

After candidate keypoints are gathered, next step is to eliminate the ones which have too low contrast level with respect to their neighbours [46]. Hence, stable keypoints appear like in Figure 3.4.

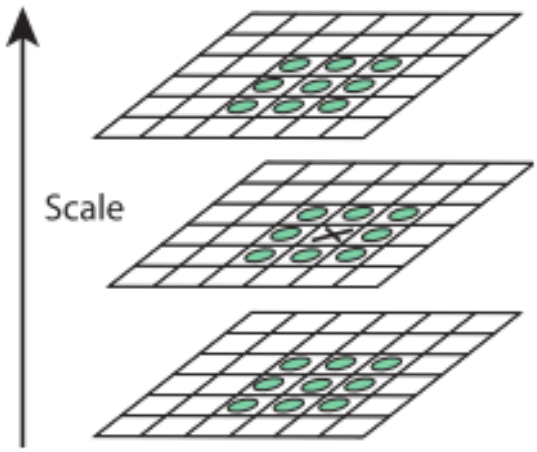

Figure 3.3. Detecting Candidate Keypoint [41].

Figure 3.4. Keypoints of Stitched Images [46].

3.1.3. Orientation Assignment and Keypoint Descriptor

Keypoint descriptor can be defined in point of assigning steady orientation to each keypoint depending on neighbourhood pixels of it [41]. Accordingly, invariance to image rotation problem can be solved. For every input image $L(x, y)$, the gradient magnitude $m(x, y)$ and orientation $\theta(x, y)$ are calculated [46]:

$$m(x,y) = \sqrt{(L(x+1,y) - L(x-1,y))^2 + (L(x,y+1) - L(x,y-1))^2} \tag{3.4}$$

$$\theta(x,y) = \arctan((L(x,y+1) - L(x,y-1))/(L(x+1,y) - L(x-1,y))) \tag{3.5}$$

A histogram is gathered by using the gradient which is calculated with respect to neighbourhood of the keypoint. The histogram has 36 bins and covers 360 degree range. Contribution of each pixel to histogram is calculated by weighting multiplication. Gradient magnitude and Gaussian-weighted circular window are used as weighting factors. The sigma of the Gaussian is 1.5 times of measure of the keypoint. Maximum peak value of the histogram and additional local peaks within 80% of the maximum peak are discovered and detected as keypoints. Lastly, parabola fitting is achieved for each chosen peaks in order to deal with interpolation and get more accurate results.

After giving location, scale and orientation to each keypoint, next stage is defining a descriptor for the regional image sections which are highly distinguishing. According to [41], it is essential to calculate the gradient magnitude and orientation for each image sample point in the area nearby the keypoint position so as to generate a keypoint descriptor such as in Figure 3.5 on the right. Gaussian window weights samples as shown by the covered circle on the left. Subsequently, samples are gathered into orientation histograms shorten the contents over 4x4 lower sections, as shown on the right in Figure 3.5. Size of each arrow is equaled to the summation of the gradient magnitudes close to that direction inside the section.

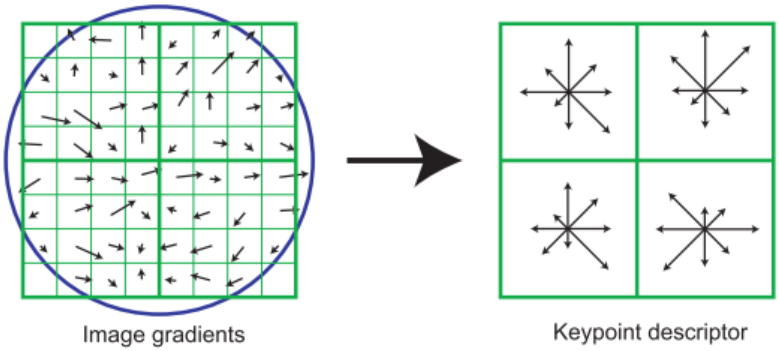

Figure 3.5. Keypoint Descriptor Gathering [46].

3.2. Homography Matrix

The images which are from the same scene but does not have the same directions could be linked by the help of homography. According to [48], homography can be

explained as follow. A pixel located at (x, y) can be transformed to (x_1, x_3, x_2) where x = x_1/x_3 and y = x_2/x_3. (x, y) point is called as homogenous representation on plane P^2. In the light of this representation, homography can be stated as a reversible mapping technique which maps points and lines on the projective plane P^2. In image stitching, determining the homography matrix is crucial since it transforms series of images, which belong to same scene, to a mutual plane where measurements can be developed [49]. In [49], homography is evaluated, after point correspondences between related planar homography and the epipolar geometry of the reference plane is acquired. Afterwards, RANSAC is run.

It is inevitable to determine 3x3 homography matrix H so as to achieve mapping. The homography matrix needs only eight degrees of freedom although it has nine components. In other words, eight unknowns should be estimated in order to determine homography matrix. Classically, homography matrix is calculated with respect to feature correspondence between two images.

According to [46], the homography transformation can be shown as below;

$$\begin{pmatrix} x_2 \\ y_2 \\ w_2 \end{pmatrix} = \begin{pmatrix} H_{11}H_{12}H_{13} \\ H_{21}H_{22}H_{23} \\ H_{31}H_{32}H_{33} \end{pmatrix} \begin{pmatrix} x_1 \\ y_1 \\ w_1 \end{pmatrix} \tag{3.6}$$

$$x_2 = Hx_1 \tag{3.7}$$

where

x_1 is position of a pixel in original image,

x_2 is position of a pixel in the merged image,

H is Homography Matrix.

For specific group of corresponding points, the final estimation of homography matrix can be acquired as below;

$$x_k = \begin{pmatrix} x_k \\ y_k \\ w_k \end{pmatrix} \qquad x_k^{'} = \begin{pmatrix} x_k^{'} \\ y_k^{'} \\ w_k^{'} \end{pmatrix}$$

where

x_k, y_k are specific keypoint positions,

w_k is 1.

After the essential derivations, the result is;

$$\begin{pmatrix} x_2 \\ y_2 \\ z_2 \end{pmatrix} = \begin{pmatrix} H_{11}H_{12}H_{13} \\ H_{21}H_{22}H_{23} \\ H_{31}H_{32}H_{33} \end{pmatrix} \begin{pmatrix} x_1 \\ y_1 \\ z_1 \end{pmatrix} \tag{3.8}$$

$$\begin{pmatrix} 0^T & -w_k^{'}x_k^T & y_k^{'}x_k^T \\ w_k^{'}x_k^T & 0^T & -x_k^{'}x_k^T \end{pmatrix} \begin{pmatrix} H_{11} \\ H_{12} \\ H_{13} \end{pmatrix} = 0 \tag{3.9}$$

Each x_k, y_k, w_k inserts two equations to the matrix A.

$$A \begin{pmatrix} H_{11} \\ H_{12} \\ H_{13} \end{pmatrix} = 0 \tag{3.10}$$

This is called Perspective Transformation or Homography and widely used in image stitching. In Perspective Transformation, one image is taken like reference image while the homographies of the other neighbour images estimated depending on reference image. As a result, other images are stitched to reference image and

panorama is obtained [46].

3.3. Random Sample Consensus

Random Sample Consensus algorithm estimates the parameters of a mathematical model by using a number of observed data. It was implemented by Fischler and Bolles [45]. According to [50], it is generally used in order to estimate homographies. Observed data has inliers and outliers. While inliers can expressed by some model parameters, outliers does not match with the model at all. RANSAC algorithm can be shortened in such a way that; first, choose randomly minimum several points essential to estimate parameters of the model, secondly, determine the number of points exceed the predefined threshold subject to concurrence with the model parameters, thirdly, if the number of inliers are bigger than the threshold re-estimate the parameters, else iterate the algorithm again [51]. It gives precise result even though there are many outliers in data and estimates the parameters rapidly. However, there is not a higher and certain bound for the iteration number [51]. M must be chosen at least one group of random points do not have outliers. In other words, the probability of having outliers should be almost equal to zero. According to [52], number of iteration can be expressed;

$$M = \frac{log(1-p)}{log(1-(1-v)^m)} \tag{3.11}$$

$$v = 1 - u \tag{3.12}$$

$$1 - p = (1 - u^m)^N \tag{3.13}$$

where

u the possibility that any certain data point is an inlier,

M iterations of the minimum count of points represented as m,

p the possibility that at least one of the sets of random samples have inliers,

v the probability of having outlier.

The parameters can be estimated from N data items.

3.4. EXPERIMENTS AND RESULTS

The stitch algorithm is tested with different conditions. Cancerous breast cell image is used as the input to test the MATLAB code. First, original image is separated into three parts, then stitching algorithm is applied.

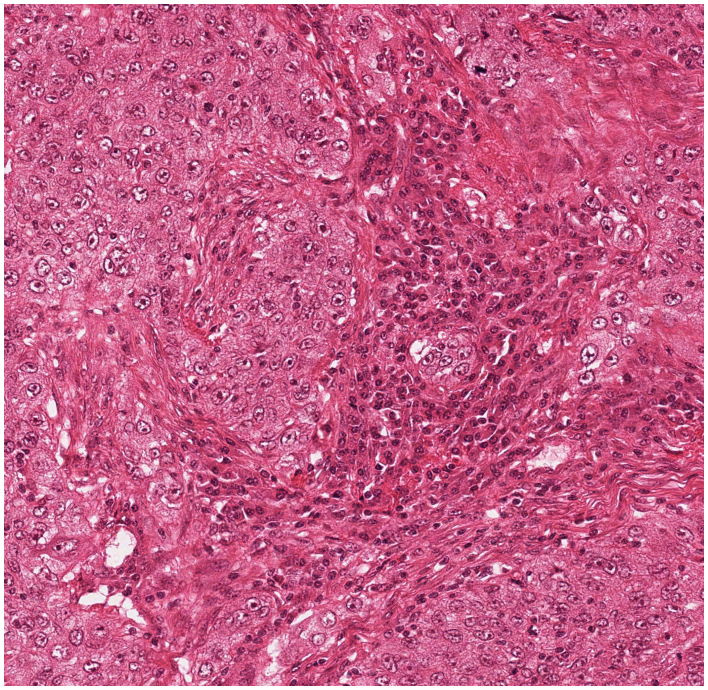

Figure 3.6. Original Cancerous Breast Cell [53].

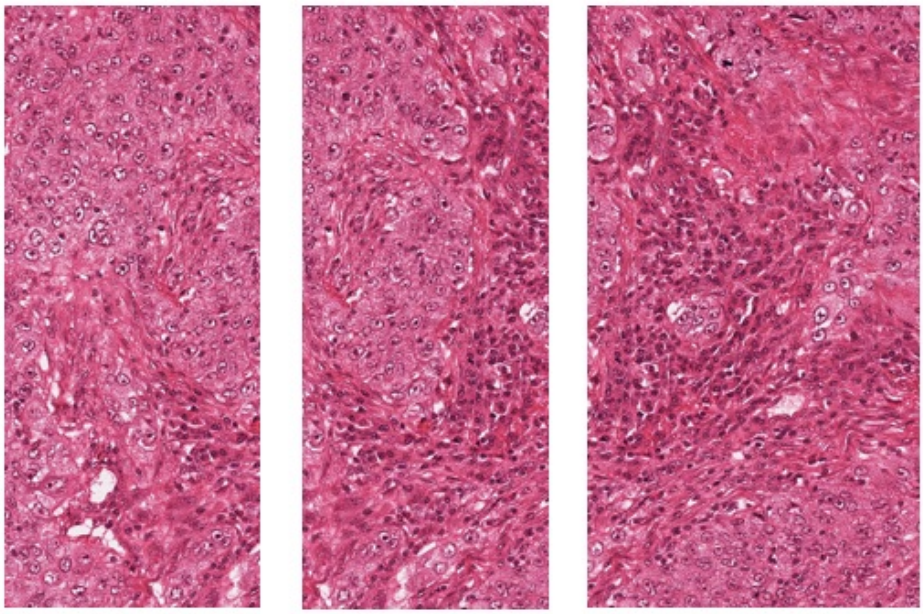

Figure 3.7. Separated Input Images.

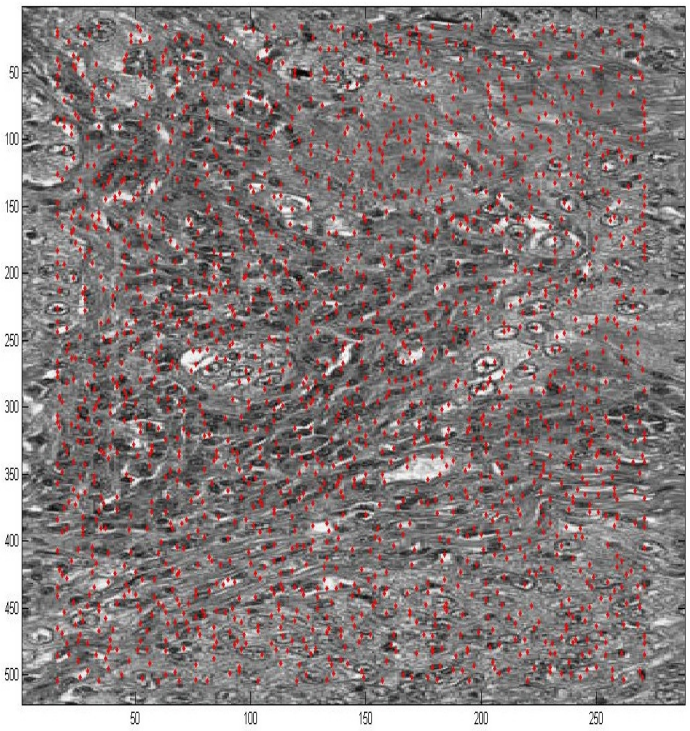

Figure 3.8. Keypoints.

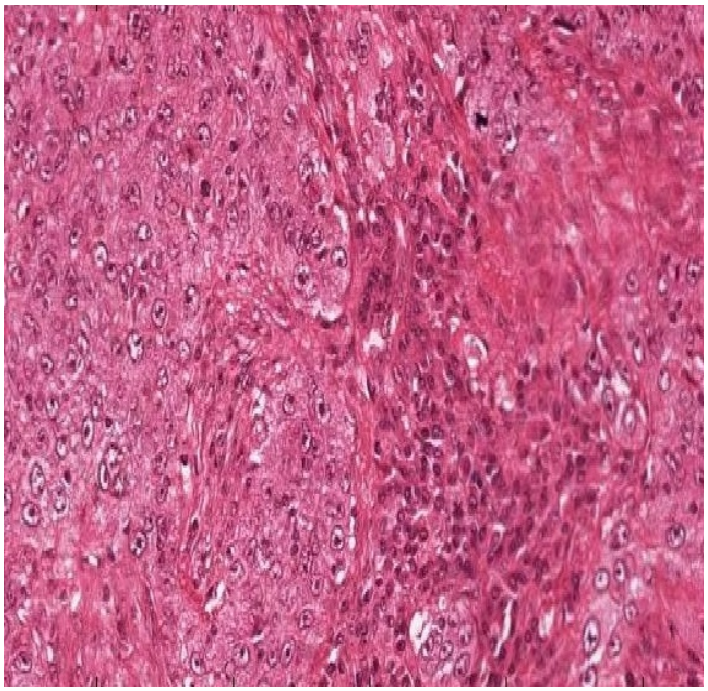

Figure 3.9. Stitched Result of Images in Figure 3.7.

Secondly, input images in Figure 3.7 are rotated five degrees with blue background color. New input images can be seen in Figure 3.10. Then, they are stitched with different combinations. Finally, irrelevant parts which belongs to background are eliminated. Both version of obtained results can be seen below in Figure 3.11, 3.12 and 3.13.

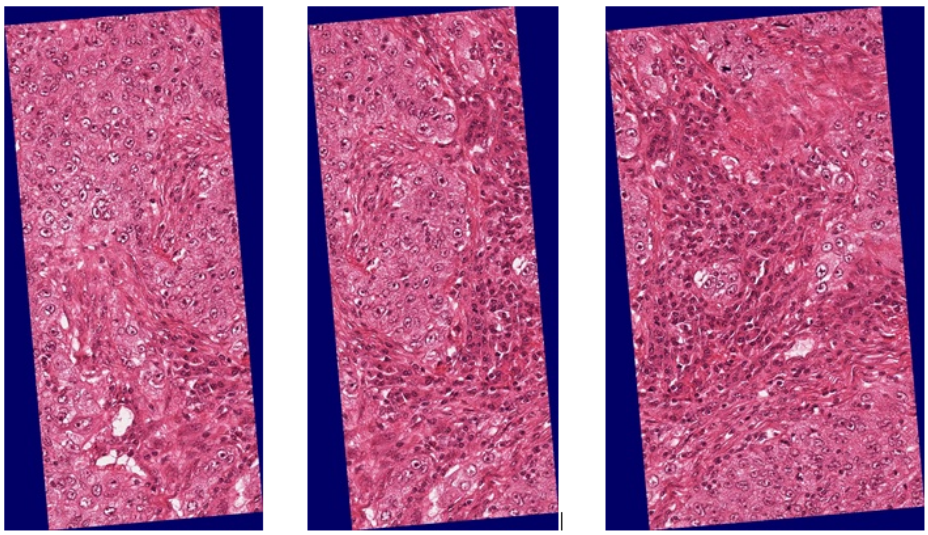

Figure 3.10. Rotated Input Images.

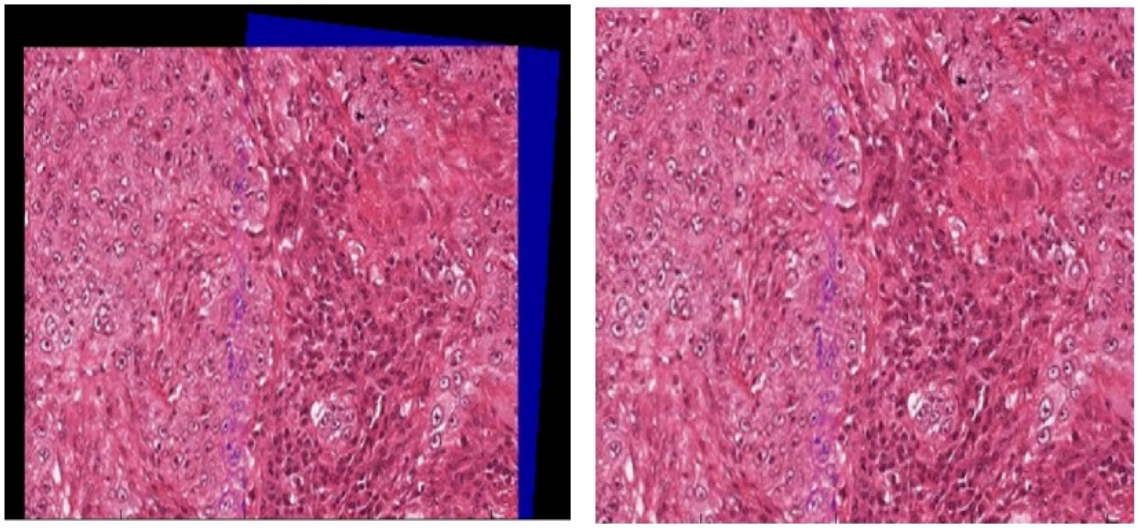

Figure 3.11. Stitched Result with Five Degrees Rotated Rightmost Input Image (left) and Result After Elimination of Irrelevant Background Color (right).

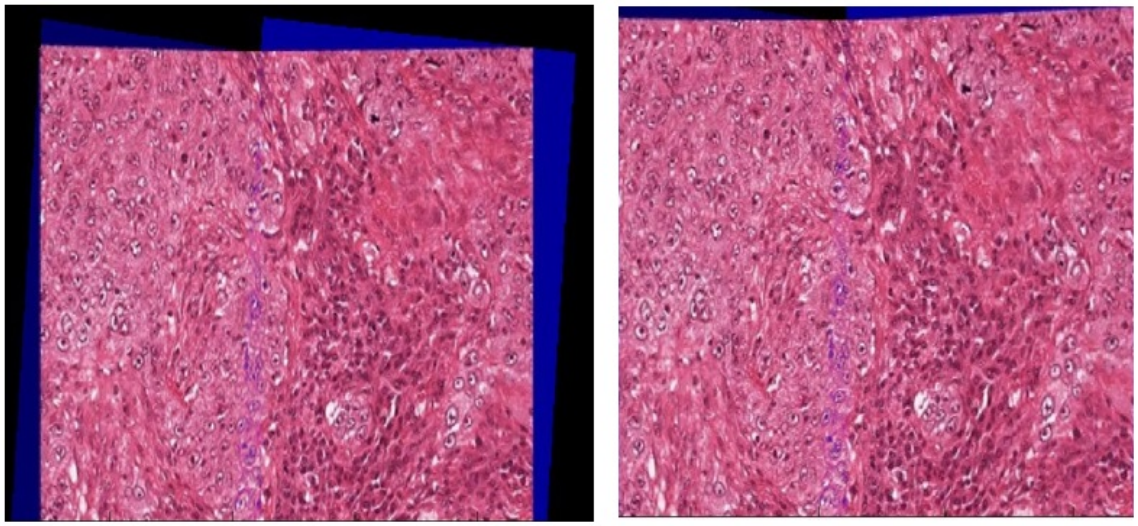

Figure 3.12. Stitched Result with Five Degrees Rotated Leftmost and Rightmost Input Image (left) and Stitched Result After Elimination of Irrelevant Background Color (right).

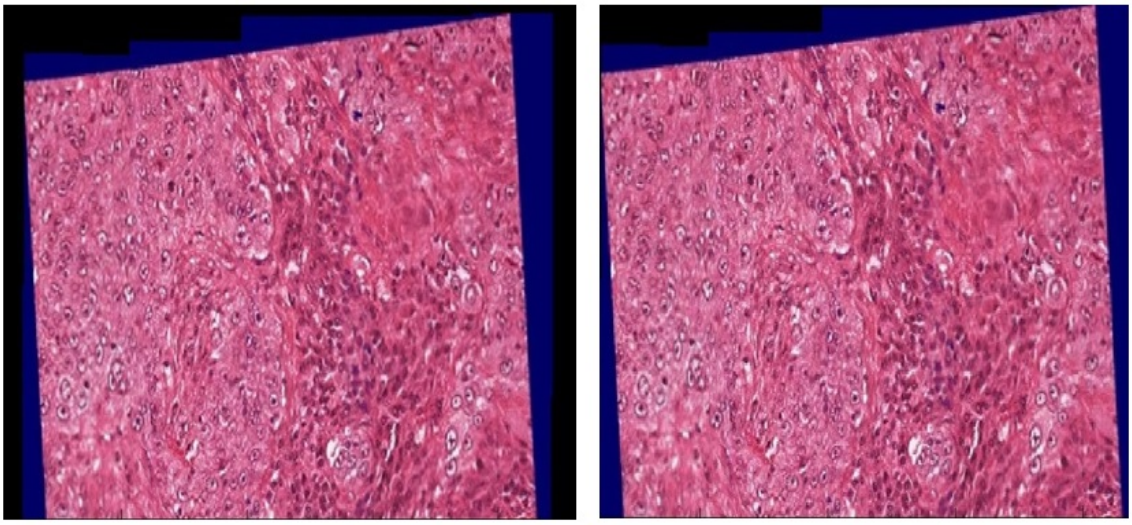

Figure 3.13. Stitched Result with Five Degrees Rotated Input Images in Figure 3.10 (left) and Result After Elimination of Irrelevant Background Color (right).

Thirdly, noise is added to input images. First salt-and-pepper noise is added to leftmost image in Figure 3.7 and then images are stitched. Next, speckle noise is added to middle image in Figure 3.7 and then images are stitched. Obtained results can be seen below in Figure 3.14 and 3.15.

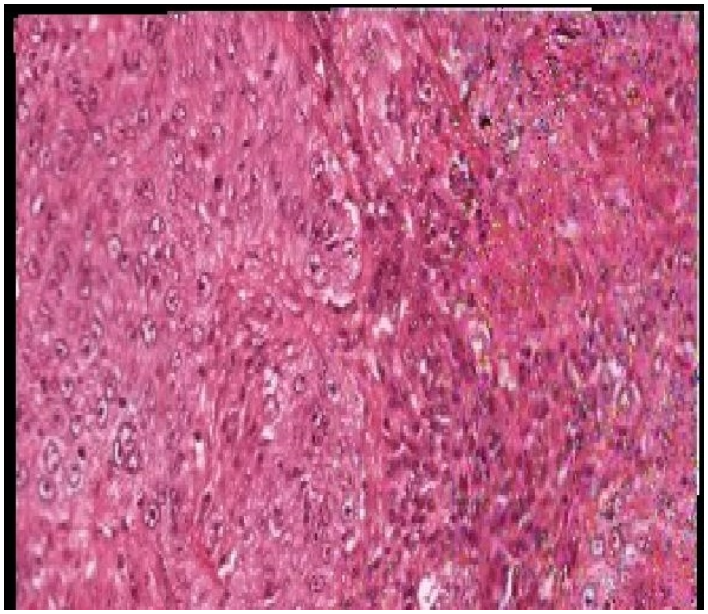

Figure 3.14. Stitched Result with Rightmost Input Image Corrupted by Salt-and-Pepper Noise (Noise Density=0.05).

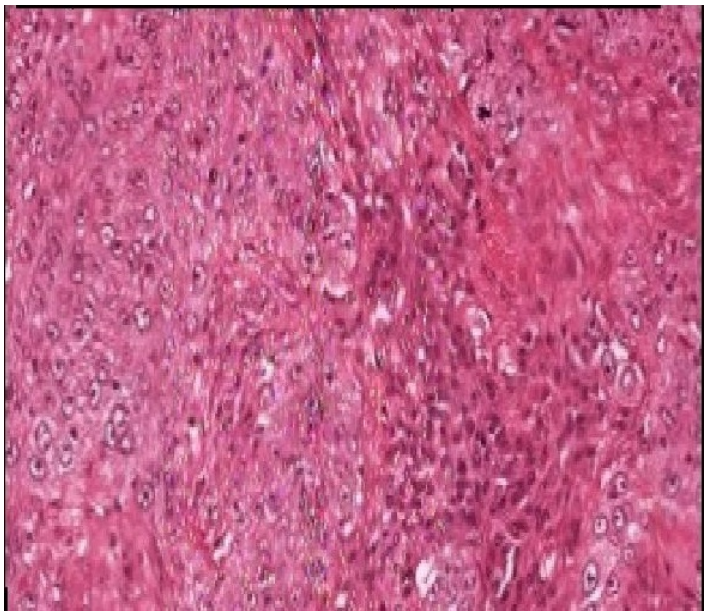

Figure 3.15. Stitched Result with Middle Input Image Corrupted by Speckle Noise (Noise Mean=0 and Variance=0.04).

3.4.1. Performance Analysis and Image Similarity

Image similarity measurement based upon image quality is a commonly used method in order to compare images. In other words, it analyses difference between original image and distorted image. In literature, there exist many types of image similarity measurement metrics. Silva *et al.* explained most of these methods in their paper [54]. Wang *et al.* offered two methods in 2002 and 2004. First one is universal image quality index (UQI) which depends on loss of correlation, luminance distortion, and contrast distortion [55]. Second one is structural similarity measurement index (SSIM) is improved version of image quality index [56]. In 2011, Zhang *et al.* improved SSIM index and offered Feature similarity index (FSIM) [57].

Investigated methods are used for the purpose of examining the performance of stitching algorithm. Although, FSIM, SSIM index and image quality index are already improved and brought into free use by authors, other methods are not. Therefore, they were improved with MATLAB. Evaluated methods are as follow; FSIM, SSIM

index, universal image quality index, Peak Mean Square Error, Average Difference, Normalized Cross-Correlation, Correlation Quality, Image Fidelity, Histogram Error Measurement, Normalized Absolute Error, Normalized Mean Square Error. Formulas for these methods can be seen as follows;

$$Q = \frac{4\sigma_{xy} + \mu_x \mu_y}{(\sigma_x^2 + \sigma_y^2)(\mu_x^2 + \mu_y^2)} \tag{3.14}$$

where

Q is universal image quality index [55],

x and y are original and test image signals.

$$SSIM(x, y) = \frac{(2\mu_x \mu_y + C_1)(2\sigma_{xy} + C_2)}{(\mu_x^2 + \mu_y^2 + C_1)(\sigma_x^2 + \sigma_y^2 C_2)} \tag{3.15}$$

where

x and y are two windows,

μ_x the mean of x,

μ_y the mean of y,

σ_x^2 the variance of x,

σ_y^2 the variance of y,

σ_{xy} the covariance of x and y,

$C_1 = (k_1 L)^2$, $C_2 = (k_2 L)^2$ two variables to balance the division with weak denominator,

L the dynamic range of the pixel-values,

$k_1 = 0.01$ and $k_2 = 0.03$ assumed [56].

$$FSIM = \frac{\sum S_L x PC_m x}{\sum PC_m x} \tag{3.16}$$

where

$$PC_m x = max(PC_1 x, PC_2 x) \tag{3.17}$$

PC is phase congruency. It detects features when Fourier elements reach maximum in phase [57].

PC_1x phase congruency of the first image,

PC_2x phase congruency of the second image,

S_Lx is similarity.

The rest of the section displays methods from [54].

$$\text{Peak Mean Square Error}(PMSE) = \frac{1}{MN}\sum_{j=1}^{M}\sum_{k=1}^{N}\frac{\left[F(j,k)-\bar{F}(j,k)\right]^2}{[max(F(j,k))]^2} \tag{3.18}$$

where

$F(j,k)$ is original image,

$\bar{F}(j,k)$ is distorted image.

$$\text{Average Difference}(AD) = \sum_{j=1}^{M}\sum_{k=1}^{N}\frac{F(j,k)-\bar{F}(j,k)}{MN} \tag{3.19}$$

$$\text{Normalized Cross-Correlation}(NK) = \frac{\sum_{j=1}^{M}\sum_{k=1}^{N}\left[F(j,k)\bar{F}(j,k)\right]}{\sum_{j=1}^{M}\sum_{k=1}^{N}\left[F(j,k)\right]^2} \tag{3.20}$$

$$\text{Correlation Quality}(CQ) = \frac{\sum_{j=1}^{M}\sum_{k=1}^{N}\left[F(j,k)\bar{F}(j,k)\right]}{\sum_{j=1}^{M}\sum_{k=1}^{N}F(j,k)} \tag{3.21}$$

$$\text{Image Fidelity}(IF) = 1 - \frac{\sum_{j=1}^{M}\sum_{k=1}^{N}\left[F(j,k)-\bar{F}(j,k)\right]^2}{\sum_{j=1}^{M}\sum_{k=1}^{N}F(j,k)} \tag{3.22}$$

$$\text{Normalized Absolute Error}(NAE) = \frac{\sum_{j=1}^{M}\sum_{k=1}^{N}|F(j,k) - \bar{F}(j,k)|}{\sum_{j=1}^{M}\sum_{k=1}^{N}|F(j,k)|} \tag{3.23}$$

$$\text{Normalized Mean Square Error}(NMSE) = \frac{\sum_{j=1}^{M}\sum_{k=1}^{N}\left[F(j,k) - \bar{F}(j,k)\right]^2}{\sum_{j=1}^{M}\sum_{k=1}^{N}\left[F(j,k)\right]^2} \tag{3.24}$$

In addition to these methods, histogram error measurement is used. It first calculates normalized histograms of two images and then calculates the sum of the squared differences between them. Two image are same if the difference is zero.

Original image in Figure 3.6 and stitched image in Figure 3.9 are used on the purpose of performance examining. The results can be seen in Table 3.1. At first column of the table, similarity between original and stitched images are compared. At second column, similarity between original image and original image are compared in order to create reference values. Every comparison belong to each method are shown in Table 3.1. The most closest values are in the histogram error measurement and normalized cross-correlation methods.

Moreover, original image in Figure 3.6 and stitched images in Figure 3.11, 3.12 and 3.13 are compared. Comparison results can be seen in Table 3.2. At the first column of the table, similarity between original image and image in Figure 3.11 are compared. At second column, similarity between original image and image in Figure 3.12 are compared. Finally, similarity between original image and image in Figure 3.13 are compared at third column. It can be recognized that irrelevant background color negatively affects the comparison. Therefore, stitched results after elimination of irrelevant background color from Figure 3.11, 3.12 and 3.13 are used for performance evaluation. However, as it can be recognized that background still has negative effect on images.

Lastly, original image in Figure 3.6 and stitched images in Figure 3.14 and 3.15

Table 3.1. Image similarity performance results.

METHOD	**Figure 3.9 & Figure 3.6**	**Figure 3.6 & Figure 3.6**
SSIM	0.9755	1
FSIM	0.6896	1
Universal Image Quality Index	0.9138	1
Average Difference	0.5753	0
Normalized Cross-Correlation	0.999	1
Correlation Quality	1.9823	1.9843
Image Fidelity	0.2124	1
Histogram Error Measurement	0.0005704	0
Normalized Absolute Error	0.1553	0
Normalized Mean Square Error	0.3969	0
Peak Mean Square Error	0.3898	0

are compared. Comparison results can be seen in Table 3.3. At first column of the table, similarity between original image and image in Figure 3.14 are compared. At second column, similarity between original image and image in Figure 3.15 are compared.

Table 3.2. Image similarity performance results with rotated input images.

METHOD	**Figure 3.6 & Figure 3.11**	**Figure 3.6 & Figure 3.12**	**Figure 3.6 & Figure 3.13**	**Figure 3.6 & Figure 3.6**
SSIM	0.9757	0.9712	0.9007	1
FSIM	0.6966	0.6612	0.5863	1
Universal Image Quality Index	0.9202	0.9015	0.8079	1
Average Difference	0.6201	1.6905	15.4275	0
Normalized Cross-Correlation	1	0.9985	0.9771	1
Correlation Quality	1.9840	1.9813	1.9388	1.9843
Image Fidelity	0.2067	0.1868	0.0506	1
Histogram Error Measurement	0.001	0.0008	0.0041	0
Normalized Absolute Error	0.1508	0.1659	0.2529	0
Normalized Mean Square Error	0.3998	0.4098	0.4785	0
Peak Mean Square Error	0.3923	0.4027	0.4722	0

Table 3.3. Image similarity performance results with noisy input images.

METHOD	**Figure 3.6 & Figure 3.14**	**Figure 3.6 & Figure 3.15**	**Figure 3.6 & Figure 3.6**
SSIM	0.9752	0.9757	1
FSIM	0.6703	0.6803	1
Universal Image Quality Index	0.913	0.9204	1
Average Difference	0.1626	1.2301	0
Normalized Cross-Correlation	0.9935	0.9984	1
Correlation Quality	1.9713	1.9811	1.9843
Image Fidelity	0.2312	0.2445	1
Histogram Error Measurement	0.0014	0.0015	0
Normalized Absolute Error	0.1541	0.1448	0
Normalized Mean Square Error	0.3874	0.3807	0
Peak Mean Square Error	0.3801	0.3733	0

4. IMAGE PROCESSING FOR CANCER DETECTION

Currently, cancer detection in image processing is a highly studied and hot topic. Generally, cancer detection methods have three main steps which are image preprocessing or enhancement, image segmentation and feature extraction. In image preprocessing part, images are passed through a set of phases in order to find image orientation, remove noise and improve the image quality. Better image enhancement process gives better results at the end.

Fundamental methods used in image preprocessing can be listed as filtering, morphological operations and histogram equalization. Briefly, there are different types of filtering techniques. Median and mean filter are used in this thesis. Another frequently used filters are; adaptive median filter used to smooth non-repulsive noise without any blurring effect while protecting the details in the image, low pass used to reduce noise but leads smoothing effect on details, high pass filter used to sharpen details in the image while reducing the noise and adaptive mean filter used to preserve the balance between homogeneous regions and edges and clean the spots on the image.

In morphological operation, each pixel value is compared with the ones in the neighbourhood. Hence, noise and high frequencies can be reduced and contrast is improved, but some part of the noise cannot be removed. There are two main morphological operations; dilation and erosion. Erosion morphological operation makes object in the image smaller with respect to selected structuring element also known as kernel. The boundaries of regions of foreground pixels are eroded. Hence, area of foreground pixels is minimized, and the holes within those areas become wider. In addition, it achieves to distinguish two object which are connected with noise in the image. Dilation operation basically expands the boundaries of regions of foreground pixels with respect to selected structuring element. As a result, area of foreground pixels enlarges while the holes within those regions become minor. It is used especially for license plate recognition, letter recognition and fingerprint recognition by reducing the noise effect.

Contrast modification is the main issue in histogram equalization. Thus, the scattering of the contrast levels becomes better as in Figure 4.1 and abnormal things become more visible. Image enhancement methods which are used in this thesis are explained in the next sections in detail.

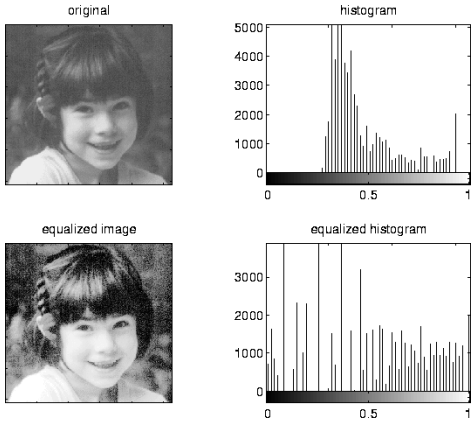

Figure 4.1. (a) Original Image and Its Histogram (b) The Equalized Image and Its Histogram [58].

The second main part of cancer detection algorithms in image processing is generally the image segmentation. It segments the image into constitute regions. Fundamental methods used in image segmentation with cancer detection can be listed as threshold technique, edge detection and watershed transform.

Threshold technique classifies image into two classes. One class is formed by the pixels which are lower than the threshold value and the other class is formed by the ones which are higher. In this thesis, Otsu's threshold technique is used [59]. In edge detection, the boundary between two associative regions also called as edge is extracted by using the different operators like Prewitt, Sobel, Roberts, Zero-cross etc. For instance, this gives the chance to identify the edges of a tumour. Moreover, Watershed transform can be used for edge detection. It depends on the watersheds in the topography. Any graylevel image may be imagined as topographic area. If the image is flooded with water from its minimum level, it can be separated two different classes; catchment basins and the watershed lines.

The third part of cancer detection algorithms is feature detection. Main purpose of feature extraction is finding abnormalities in the image which was passed through image enhancement and segmentation processes. Frequently used two methods are binarization and masking approach [60]. In binarization method, image is binarized by extracting the brightness and density. In masking method, a mask matrix is convolved with original image.

Kumar *et al.* [60] used some of mentioned methods in order to find nodules in the lungs and make diagnosis earlier by using X-Ray images. They first applied image preprocessing and then feature extraction. Similarly, Gopinath [61] used high pass and median filter with morphological operations, threshold technique and watershed segmentation to detect prostate cancer.

However, these mentioned studies and most of them in the literature are based on only the images. In other words, result of these studies are still images which can interpreted only by the professions. In this thesis, two different kinds of subjective classifiers are proposed. Unlike the general literature, since the result are based on statistical data and numbers, anyone can deduce from the test result whether the image is cancerous one or not. Another novelty is about types of proposed classifiers. First one is calculating the Root Means Square Error in point of line plots and the second one is detecting cancer tissue by using the histogram. Detailed information about steps and flow chart are given in Figure 4.3.

According to [62], correlation between human age and cell structure can be analysed by using Fourier transform. In vivo human corneal endothelial cells were used for the analysis. [63] used the proposed method with multiphoton laser scanning microscopy images and implemented an algorithm. In this thesis, further method is developed by using mentioned studies in [62] and [63].

Firstly, line plot of the center row of the image in the Fourier domain is plotted as in [63]. It is observed that line plot belongs to healthy images are symmetric unlike the cancerous images. In order to measure symmetry of the line plot, RMSE value for

both type of images and accuracy are calculated. Therefore, the performance of the classifiers is deduced by evaluating the accuracy.

Secondly, improved histogram-based classifier identifies the image with respect to comparison of the total number of dark and light pixels. It can be seen in Figure 4.2 that, cervical intraepithelial neoplasia (CIN) cancer images have darker pixel values than benign image since cancer images have many cell nucleus. This becomes more visible as cancer expands.

A similar study is conducted by Li *et al.* in 2012 [64]. However, histogram-based Gaussian Mixture Modal is used to detect breast cancer. GMM weights each pixel in the image and creates complex distribution since single Gaussian distribution is not enough to display a complex distribution. They used Expectation Maximization method to calculate the parameters of GMM for both training and test images. Expectation Maximization estimates the unknown parameters by looking at the given data. First, they calculated GMM parameters for both training and test images and then computed the similarity between parameters for classification. Another histogram-based classifier is improved by Chapelle *et al.* [65]. In the study, histogram is used as input to Support Vector Machine (SVM). It is an overseen learning model which examines data and recognizes pattern. Alternative way of using histogram for breast cancer classification is offered by Nithya and Santhi in 2011 [66]. In the study, intensity histogram features which are smoothness, uniformity, third moment and entropy are calculated, and then they are compared for healthy and cancerous image classes.

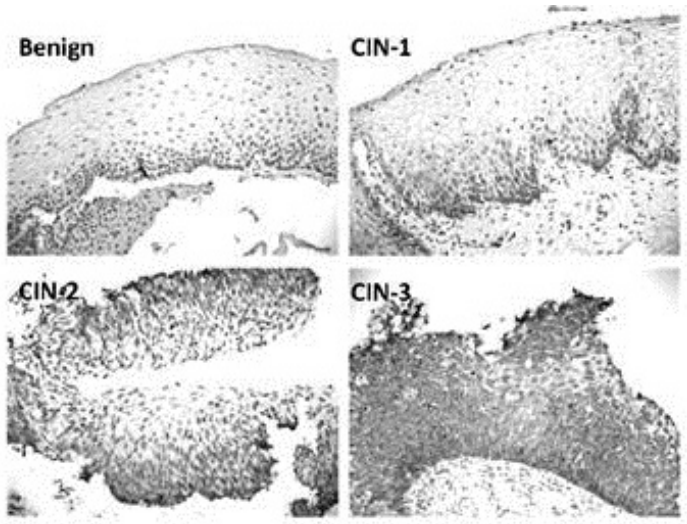

Figure 4.2. Different IMP2 Staining Patterns in Benign, CIN-1, CIN-2 and CIN-3 Lesions [67].

Unlike mentioned studies above, histogram is not used as input or a tool in this thesis, instead it is used directly to classify the images. Moreover, different types of cancer images, i.e. not only one type of cancer, are put account as input. In conclusion, performance of classifiers is determined.

4.1. Median Filter

The first step of the proposed approaches is median filtering shown in Figure 4.3. The median filter evaluates each pixel in the image respectively and looks at their close by neighbours. The median is calculated by categorizing the pixel values nearby neighbourhood into numerical order, and then the pixel being analysed is changed with the middle -mean- pixel value. The main advantage of median filter is that it removes noise while keeping the edges since edges. However, if the number of noisy pixels in a window is higher than or equal to the half of non-noisy pixel number, median filter does not give good results.

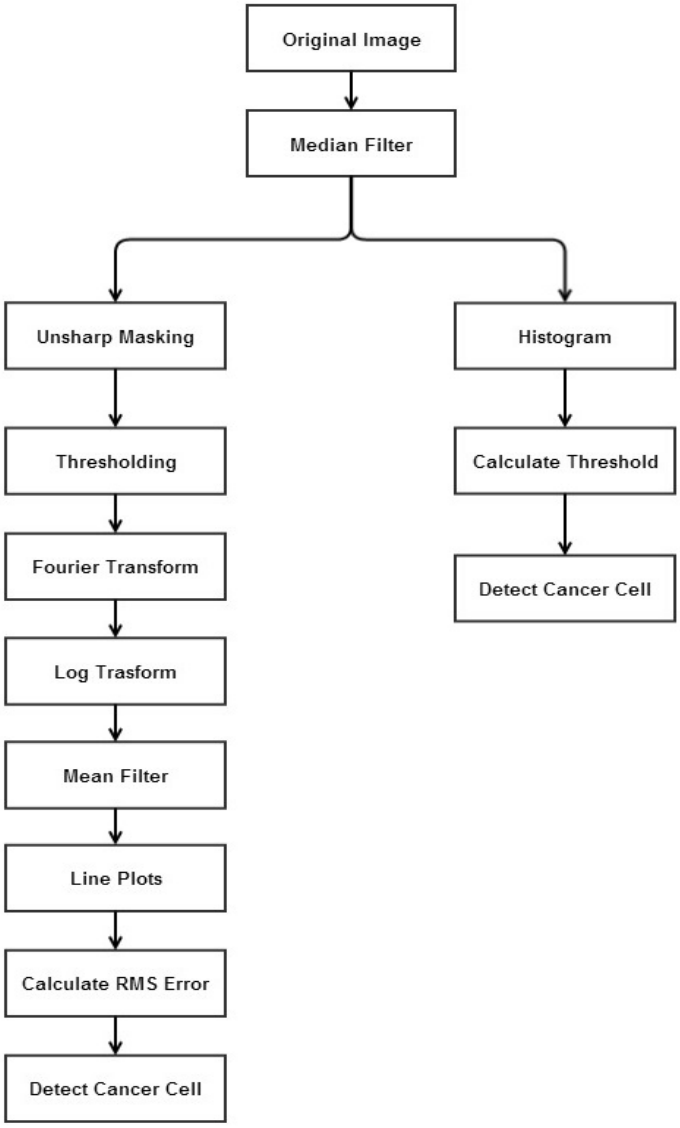

Figure 4.3. Cancer Detection Flow Chart.

4.2. Unsharp Masking

Unsharp filtering is used in order to clarify sharp transitions and details in the image. It is achieved by subtracting an unsharp, or smoothed, form of an image from the original image.

4.3. Thresholding

Thresholding is the basic image processing function in segmentation. In this thesis, OTSU's threshold method is used [59]. It assigns 0 or 1 to each pixel in the image by comparing the threshold pixel value which is determined by the user. In this way, the image is converted from gray level image to binary image.

4.4. Fourier Transform

Two-dimensional Discrete Time Fourier transform of binary images is calculated in MATLAB in order to pass them from spatial domain to frequency domain. The formula is given below;

$$F(w,z) = \sum_{m=-\infty}^{\infty} \sum_{n=-\infty}^{\infty} f(m,n) e^{-2\pi j(mw+nz)} \tag{4.1}$$

where
w and z are spatial frequencies in x and y directions respectively,
$F(w,z)$ is the 2D spectrum of $f(x,y)$.

4.5. Log Transform

Log transform decreases the value of light pixels and increases the values of dark pixels of the image. This procedure clears the details of the transform and makes it more distinct.

4.6. Mean Filter

Mean filter uses the similar manner with median filter; however, instead of replacing the pixel with median value, it replaces the pixel with the mean value. After log transform step, mean filter is used in order to reduce sharp transition between gray levels. As a result of this, image becomes blurred.

4.7. Line Plot

In order to analyse the image in statistical signal processing manner, the center row of the mean filtered image is extracted and plotted in MATLAB. It is observed that healthy tissue images have even function distribution. On the contrary, cancerous images have irregular distribution.

4.8. Root Mean Square Error

After images are passed through image enhancement and segmentation steps, two different classifier are used. First one is based on Root Mean Square Error (RMSE). It is a numerical measure of the degree of a changing quantity in statistics. In this thesis, RMSE is used to measure the symmetry of the line plots. As it was mentioned at previous section, the line plot of the healthy image behaves like even function which means it is symmetric. On the other hand, cancerous images do not behave like even function. In the light of this information, a hypothesis is established. RMSE of the line plot of the cancerous image should be bigger than the line plot of the healthy image, since it is less symmetric. In order to evaluate RMSE, the line plot is separated to two parts at the center. After, RMSE is calculated with respect to differences between reciprocal pixel values; for instance, difference between i^{th} and $[n-i]^{th}$ pixel values where n is the maximum value of the pixel number and i is random pixel number which is less than or equal to n. The formula of normalized RMSE is as follow;

$$RMSE = \sqrt{\frac{\sum_{i=1}^{n} \left(x_i - x_i^{'}\right)^2}{n}} \tag{4.2}$$

where

n is the total number of pixels,

x_i value of the pixel,

$x_i^{'}$ reciprocal pixel value.

4.9. Finding Threshold for Histogram

First of all, histogram of cancer and healthy images are calculated. After that, different thresholds are found in order to divide overall histogram into two parts such as dark pixels group and light pixels group. Since cancerous tissue is denser, it has also darker pixels than healthy tissue. An example can be seen in Figure 4.2. In this algorithm 13 different threshold methods [68, 69] are used.

The histogram is represented as $y_0, y_1, ..., y_n$, where
t is threshold,
n is the total number of pixels,
i is the number of gray levels in the image,
y_i is the number of pixels in the image with gray level i.

4.9.1. Minimum

The minimum method chooses the threshold to be in the valley of the bimodal histogram. It is also known as the mode method. In bimodal distributions, there are two remarkable and different peak values. One way to do this is setting all of the y_i values to $\frac{y_{i-1}+y_i+y_{i+1}}{3}$ for $i = 0, 1, ..., n$ and $y_{-1} = y_{n+1} = 0$. This operation is repeated until y's become bimodal. Finally, t is equated to i value which makes y_i minimum such that $y_{t-1} > y_t \leq y_{t+1}$.

4.9.2. Intermodes

The intermodes method calculates the threshold with mean of two peaks (y_k and y_j) of the bimodal histogram.

$$t = \frac{j + k}{2} \tag{4.3}$$

Following partial sums should be obtained in order to achieve next threshold

methods.

$$A_j = \sum_{i=0}^{j} y_i \qquad B_j = \sum_{i=0}^{j} i y_i \qquad C_j = \sum_{i=0}^{j} i^2 y_i \tag{4.4}$$

where $j = 0, 1, ..., n$.
These equations are calculated iteratively such as in equation 4.5.

$$A_j = A_{j-1} + y_j \tag{4.5}$$

4.9.3. Median

The median method calculates the threshold by assuming that half of the pixels belongs to the background and the other half belongs to the foreground. It is very useful when there is not enough information about the background and foreground parts. In this case, 50 percent of data is assumed one group and 50 percent of data is assumed the other group.

4.9.4. Ptile

The ptile method assigns t when the value of $\frac{A_t}{A_n}$ is as close as possible to 0.5.

4.9.5. Mean

The mean method basically calculates mean of the pixels in the image. This method assigns t the value of integer part of the $\frac{B_n}{A_n}$.

4.9.6. Moments

The moments method assigns t when the value of $\frac{A_t}{A_n}$ is as close as possible to x_0.

$$x_0 = \frac{1}{2} - \frac{\frac{B_n}{A_n}}{\sqrt{x_2^2 - 4x_1}} \qquad x_1 = \frac{B_n D_n - C_n^2}{A_n C_n - B_n^2} \qquad x_2 = \frac{B_n C_n - A_n D_n}{A_n C_n - B_n^2} \tag{4.6}$$

$$D_n = \sum_{i=0}^{n} i^3 y_i \tag{4.7}$$

4.9.7. Entropy

The entropy method calculates entropy of image histogram. Threshold value is made equal to j value which makes the equation 4.9 maximum.

$$E_j = \sum_{i=0}^{j} y_i \log y_i \tag{4.8}$$

$$\frac{E_j}{A_j} - \log A_j + \frac{E_n - E_j}{A_n - A_j} - \log A_n - A_j \tag{4.9}$$

where $j = 0, ..., n-1$.

4.9.8. Intermeans Iteration

First of all, an initial guess is assigned to t. Afterwards, equation 4.10 and 4.11 are calculated for both of the group which is separated by the initial threshold value.

$$\mu_t = \frac{A_t}{B_t} \tag{4.10}$$

$$\nu_t = \frac{B_n - B_t}{A_n - A_t} \tag{4.11}$$

Finally, the last value of the threshold is calculated by using mean of these two means. All of these equations are calculated iteratively until t converges one specific value.

$$t = \frac{\mu_t + \nu_t}{2} \tag{4.12}$$

4.9.9. Intermeans

The intermeans method is commonly known as Otsu's method [59]. Threshold value is made equal to j value which makes the equation 4.13 maximum.

$$A_j(A_n - A_j)(\mu_j - \nu_j)^2 \tag{4.13}$$

where $j = 0, ..., n-1$.

4.9.10. Minerror Iteration

First of all, equation 4.14, 4.15, 4.16 and 4.17 are solved by using the initial guess for t. After that, second order equation 4.18 is solved. Integer part of the result is assigned to t. These calculations continue until t converges a value and second order equation could not have any real root.

$$\sigma_t^2 = \frac{C_t}{A_t} - \mu_t^2 \tag{4.14}$$

$$\tau_t^2 = \frac{C_n - C_t}{A_n - A_t} - \nu_t^2 \tag{4.15}$$

$$\rho_t = \frac{A_t}{A_n} \tag{4.16}$$

$$q_t = \frac{A_n - A_t}{A_n} \tag{4.17}$$

$$x^2 \left\{ \frac{1}{\sigma^2} - \frac{1}{\tau^2} \right\} - 2x \left\{ \frac{\mu}{\sigma^2} - \frac{\nu}{\tau^2} \right\} + \left\{ \frac{\mu}{\sigma^2} - \frac{\nu}{\tau^2} + \log \frac{\sigma^2 q^2}{\tau^2 \rho^2} \right\} = 0 \tag{4.18}$$

4.9.11. Minerror

Threshold value is made equal to j value which makes the equation 4.19 minimum. Error is minimized in this way.

$$\rho_j \log \frac{\sigma_j}{\rho_j} + q_j \log \frac{\tau_j}{q_j} \tag{4.19}$$

where $j = 0, ..., n-1$.

4.9.12. Maxlike

The maxlike method uses maximum likelihood via expectation maximization. Initial guesses are assigned to $\mu, \sigma^2, \tau^2, \upsilon, \rho$ and q. For example, results were calculated at previous methods. After that, equations below are iteratively solved until each variable converges one specific value. Finally, the equation 4.18 is solved so as to find threshold.

$$y_i = 1 - \phi_i \qquad F = \sum_{i=0}^{n} \phi_i \gamma_i \qquad G = \sum_{i=0}^{n} y_i \gamma_i \tag{4.20}$$

$$\rho = \frac{F}{A_n} \qquad q = \frac{G}{A_n} \qquad \mu = \sum_{i=0}^{n} \frac{(i \phi_i \gamma_i)}{F} \tag{4.21}$$

$$\upsilon = \sum_{i=0}^{n} \frac{(iy_i\gamma_i)}{G} \qquad \sigma^2 = \sum_{i=0}^{n} \frac{i^2\phi_i\gamma_i}{F} - \mu^2 \qquad \tau^2 = \sum_{i=0}^{n} \frac{i^2 y_i\gamma_i}{G} - \upsilon^2 \tag{4.22}$$

where $i = 0, ..., n$.

4.9.13. Concavity

The concavity method chooses the threshold from shoulder of the histogram. First of all, histogram of the image and convex hull of the histogram are calculated. Convex hull of a bunch of points in the Euclidean plane is the minimum convex set which includes these points. Then, convex hull is subtracted from the histogram. Candidate threshold values are local maximum points of this calculation [70]. Since large concavities can also have noise spikes, each possible threshold value cannot be good applicant. These are called as spurious concavities. Balance measure which is shown in equation 4.23 is done to get rid of spurious concavities.

$$E_i = \left\{ \sum_{j=g_0}^{g_i-1} h(j) \right\} \left\{ \sum_{j=g_i}^{g_{l-1}} h(j) \right\} \tag{4.23}$$

where

$g_0, g_1, ..., g_{l-1}$ are set of gray levels,

$h(g_0), h(g_1), ..., h(g_{l-1})$ the height of the histogram at these gray levels.

Balance measure of spurious concavities is a small value. Therefore, the one which has the maximum balance measure is chosen as threshold.

4.10. EXPERIMENTS AND RESULTS

Cancer and healthy input images are gathered from [53, 71–75]. They are used in order to test performance of proposed approaches. In image pair in Figure 4.4, there

are one healthy breast and one cancerous breast tissue image. Outcomes of each step in Figure 4.3 are seen on those images step by step in the next sections.

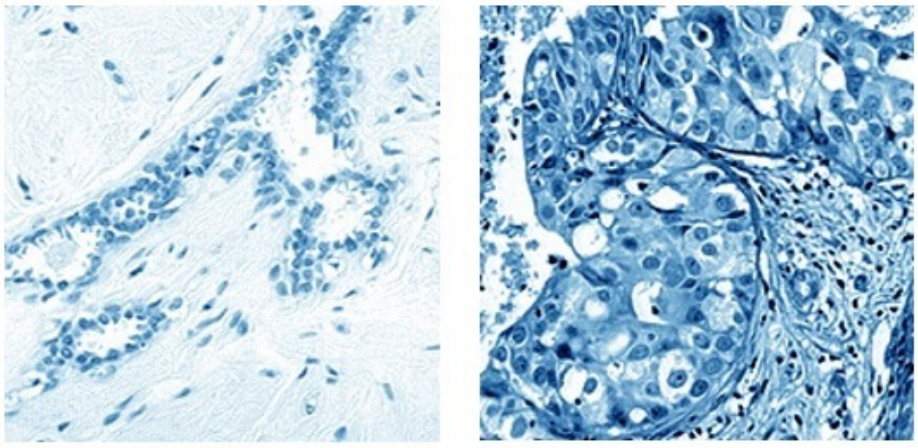

Figure 4.4. Healthy Breast Tissue(left) and Cancerous Breast Tissue(right) [73].

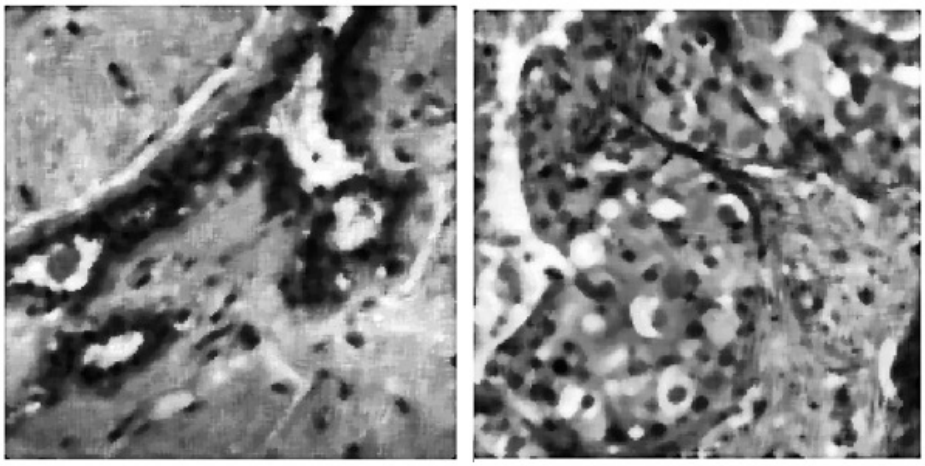

Figure 4.5. Healthy Breast Tissue(left) and Cancerous Breast Tissue(right) After Median Filtering.

First, images are converted from RGB to binary and then median filter eliminated noise while preserving important edges in the images.

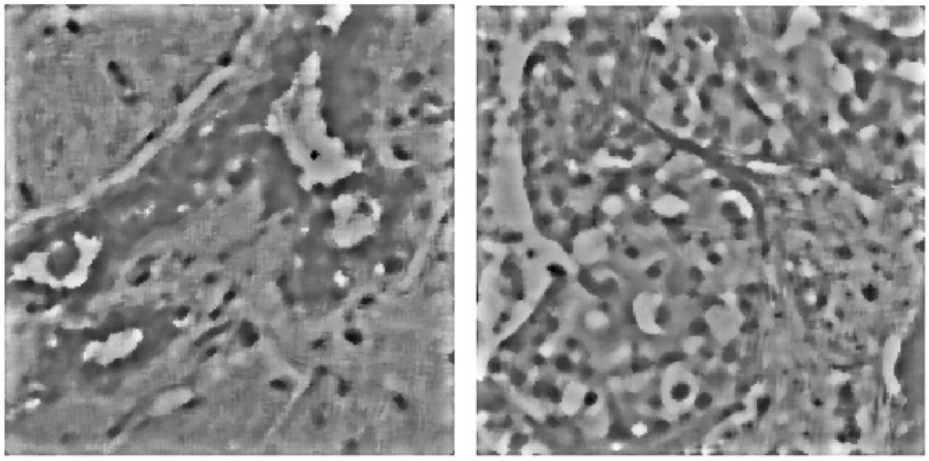

Figure 4.6. Healthy Breast Tissue(left) and Cancerous Breast Tissue(right) After Unsharp Masking.

Unsharp masking is applied to clarify the sharp transitions and make details more clear.

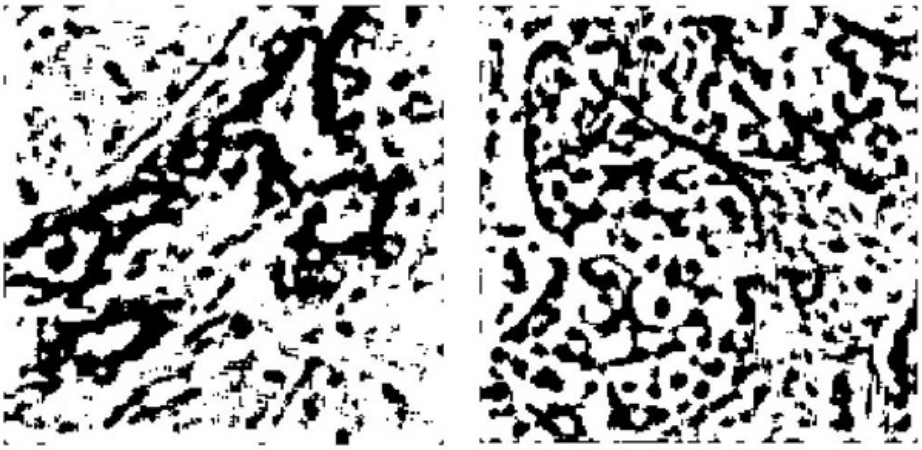

Figure 4.7. Healthy Breast Tissue(left) and Cancerous Breast Tissue(right) After Threshold Segmentation.

As it was mentioned in the introduction part, cancerous cells have more than one nuclei and denser structure. Otsu's threshold method is applied here to reveal it. According to Otsu, pixels bigger than threshold are equated to 1, pixels less than threshold are equated to 0 [59].

Figure 4.8. Healthy Breast Tissue(left) and Cancerous Breast Tissue(right) After Fourier Transform.

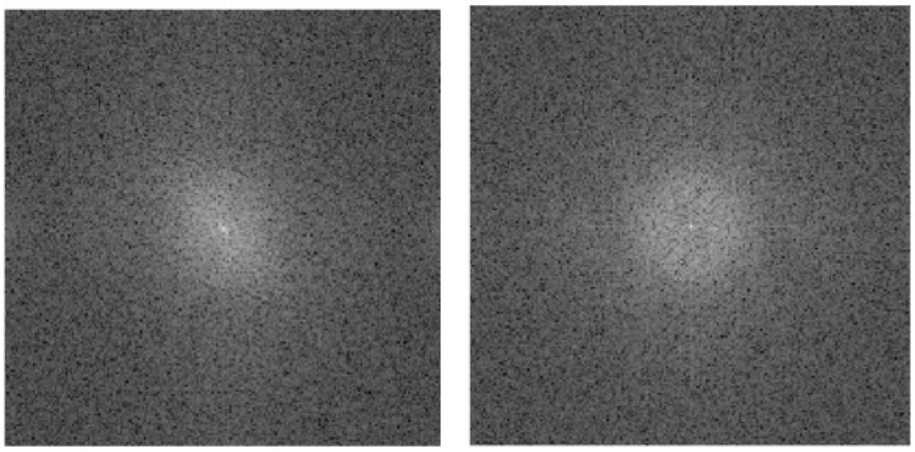

Figure 4.9. Healthy Breast Tissue(left) and Cancerous Breast Tissue(right) After Log Transform.

The values of light pixels are increased and the values of dark pixels are decreased by the help of Logarithmic transforms. Therefore, difference between foreground and background is made distinct.

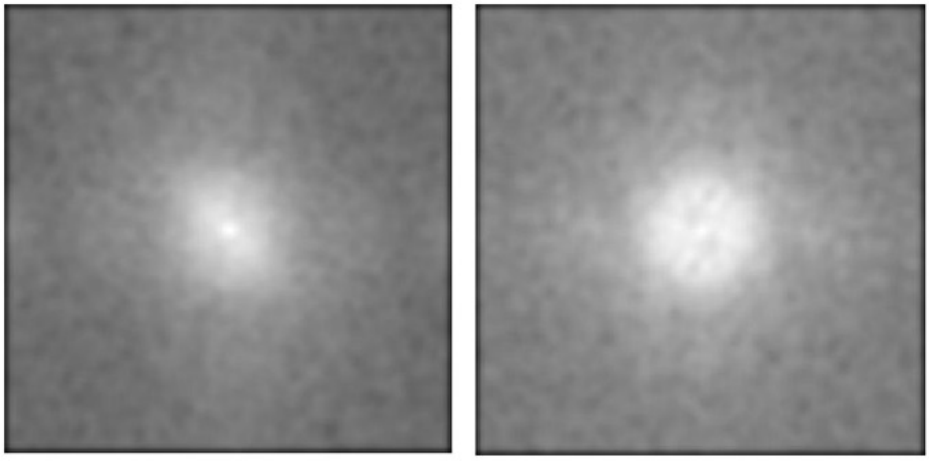

Figure 4.10. Healthy Breast Tissue(left) and Cancerous Breast Tissue(right) After Mean Filtering.

Finally before classification steps, sharp transitions are softened by the mean filter.

4.10.1. Performance Analysis of RMSE Based Classifier

Line plots are used to evaluate performance of RMSE approach. As it can be observed, healthy breast tissue has a symmetric line plot while cancerous one does not. In order to measure level of symmetry, RMSE can be calculated. According to proposed approach in this thesis, RMSE of the line plot of the healthy image should be less than cancerous one. In other words, healthy image should be more symmetrical than cancerous.

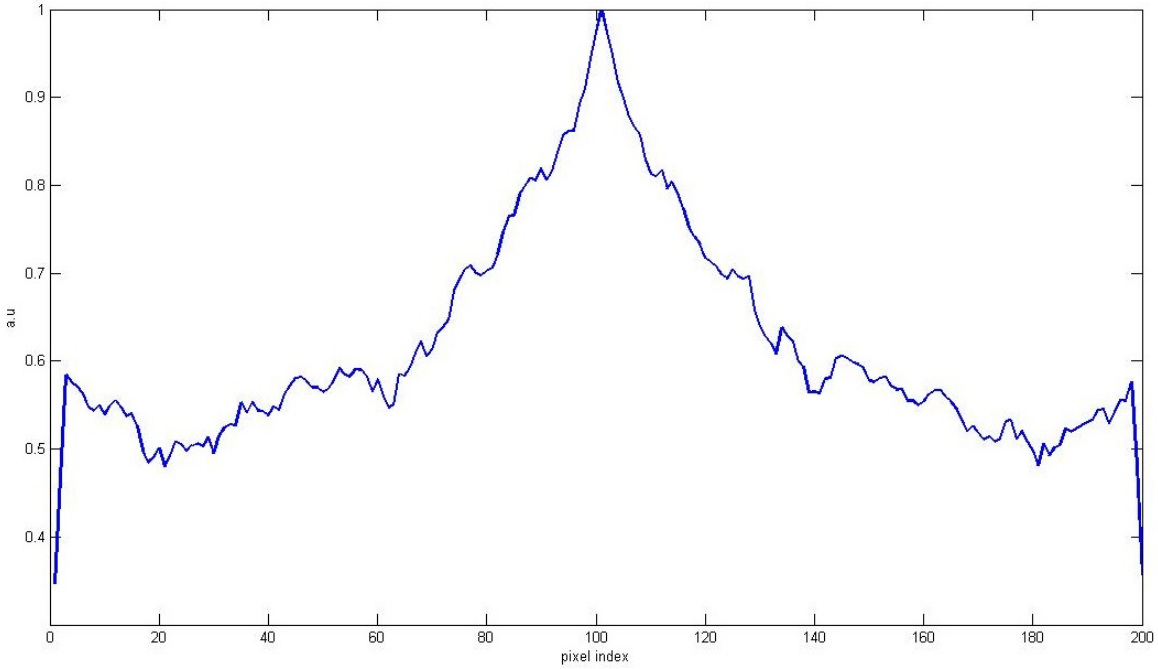

Figure 4.11. Line plot of Healthy Breast Tissue.

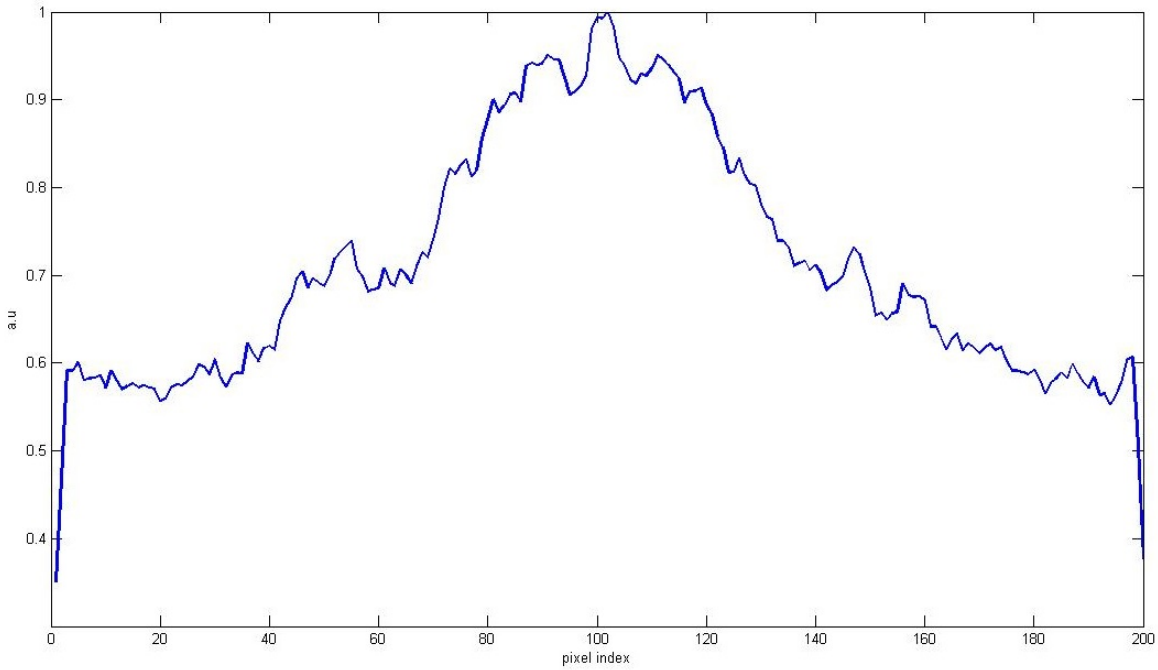

Figure 4.12. Line plot of Cancerous Breast Tissue.

Outcome of the test for sixteen different image pair is listed in Table 4.1. Nine image pair detected correctly. Accuracy of the classifier could be calculated as follows.

$$\text{Accuracy } (\%) = \frac{\text{Number of Correct Classification}}{\text{Number of Total Classification}} * 100 \tag{4.24}$$

Hence, it is equal to 56.25 %.

$$\text{Accuracy } (\%) = \frac{9}{16} * 100 = 56.25\% \tag{4.25}$$

Table 4.1. Schematic of the outcome of the RMSE classifier.

	OUTCOME
Healthy Cell RMSE <= Cancerous Cell RMSE	9
Healthy Cell RMSE > Cancerous Cell RMSE	7
TOTAL	16

4.10.2. Performance Analysis of Histogram Based Classifier

Separating two different classes perfectly with a specific test is not possible. Moreover, distributions of the test outcomes can overlap as in Figure 4.13 and performance values change depending upon each different threshold value. At this point, True Positive (TP) expresses true diagnosis of cancer. It gives cases with cancer correctly detected as positive. False Positive (FP) expresses wrong diagnosis of cancer or gives cases classified as cancer while the patient is healthy. False Negative (FN) gives cases classified as healthy while the patient has cancer. True Negative (TN) gives cases classified as healthy while the patient is healthy.

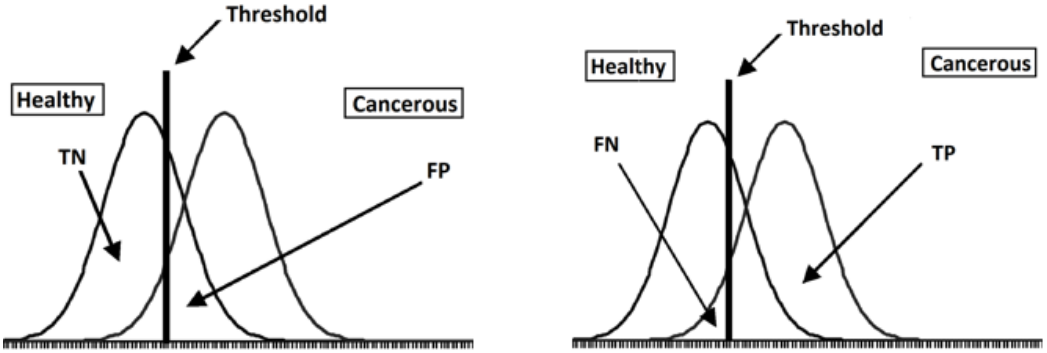

Figure 4.13. Distribution of the Test Outcomes.

There are some other evaluation criteria to analyse the test performance. First one sensitivity, indicates the probability of an outcome is positive while the cancer is present. In other words, it displays the percentage of true detection of cancer between cancerous patients. Secondly, specificity measures the probability of an outcome is negative while the cancer is not present. Both sensitivity and specificity should be

Table 4.2. Schematic of the outcome of the test.

	OUTCOME		TOTAL
METHOD	Cancerous	Healthy	
Positive Result	True Positive (TP)	False Positive (FP)	TP + FP
Negative Result	False Negative (FN)	True Negative (TN)	FP + TN
TOTAL	TP + FN	FP + TN	

calculated in order to evaluate the test efficiency. Another evaluation criteria, positive likelihood ratio is the ratio between true positive and false negative or the ratio between sensitivity and 1-specificity. Negative likelihood ratio is the ratio between false negative and true negative or the ratio between 1-sensitivity and specificity. Positive predictive value is the probability of cancer is present when the outcome is positive. Negative

predictive value is the probability of cancer is not present when the outcome is negative.

$$\text{Sensitivity} = \frac{\text{TP}}{\text{TP} + \text{FN}} \qquad \text{Specificity} = \frac{\text{TN}}{\text{TN} + \text{FP}} \tag{4.26}$$

$$\text{Positive Likelihood Ratio} = \frac{\text{Sensitivity}}{1 - \text{Specificity}} \tag{4.27}$$

$$\text{Negative Likelihood Ratio} = \frac{1 - \text{Sensitivity}}{\text{Specificity}} \tag{4.28}$$

$$\text{Positive Predictive Value} = \frac{\text{TP}}{\text{TP} + \text{FP}} \tag{4.29}$$

$$\text{Negative Predictive Value} = \frac{\text{TN}}{\text{FN} + \text{TN}} \tag{4.30}$$

The tests are applied to thirty five cancerous and thirteen healthy images. Each table in below belongs to one type of threshold method. There are two column show the real situation of the subjects, cancerous or healthy. The rows display the outcome of the test, positive or negative.

Table 4.3. Results of classifier with concavity threshold and actual outcome.

	OUTCOME		TOTAL
CONCAVITY	Cancerous	Healthy	
Number of dark pixel > Number of light pixel	14	6	21
Number of dark pixel <= Number of light pixel	21	7	27
TOTAL	35	13	

Table 4.4. Results of classifier with entropy threshold and actual outcome.

	OUTCOME		TOTAL
ENTROPY	Cancerous	Healthy	
Number of dark pixel > Number of light pixel	32	1	33
Number of dark pixel <= Number of light pixel	3	12	15
TOTAL	35	13	

Table 4.5. Results of classifier with intermeans threshold and actual outcome.

	OUTCOME		TOTAL
INTERMEANS	Cancerous	Healthy	
Number of dark pixel > Number of light pixel	11	4	15
Number of dark pixel <= Number of light pixel	22	9	31
TOTAL	35	13	

Table 4.6. Results of classifier with intermeans iteration threshold and actual outcome.

	OUTCOME		TOTAL
INTERMEANS ITERATION	Cancerous	Healthy	
Number of dark pixel > Number of light pixel	20	6	27
Number of dark pixel <= Number of light pixel	15	7	21
TOTAL	35	13	

Table 4.7. Results of classifier with intermodes threshold and actual outcome.

	OUTCOME		TOTAL
INTERMODES	Cancerous	Healthy	
Number of dark pixel > Number of light pixel	13	7	20
Number of dark pixel <= Number of light pixel	22	6	28
TOTAL	35	13	

Table 4.8. Results of classifier with maxlike threshold and actual outcome.

	OUTCOME		TOTAL
MAXLIKE	Cancerous	Healthy	
Number of dark pixel > Number of light pixel	19	7	26
Number of dark pixel <= Number of light pixel	16	6	22
TOTAL	35	13	

Table 4.9. Results of classifier with mean threshold and actual outcome.

	OUTCOME		TOTAL
MEAN	Cancerous	Healthy	
Number of dark pixel > Number of light pixel	19	6	26
Number of dark pixel <= Number of light pixel	16	7	22
TOTAL	35	13	

Table 4.10. Results of classifier with median threshold and actual outcome.

	OUTCOME		TOTAL
MEDIAN	Cancerous	Healthy	
Number of dark pixel > Number of light pixel	0	0	0
Number of dark pixel <= Number of light pixel	35	13	48
TOTAL	35	13	

Table 4.11. Results of classifier with minerror threshold and actual outcome.

	OUTCOME		TOTAL
MINERROR	Cancerous	Healthy	
Number of dark pixel > Number of light pixel	35	6	41
Number of dark pixel <= Number of light pixel	0	7	7
TOTAL	35	13	

Table 4.12. Results of classifier with minerror iteration threshold and actual outcome.

	OUTCOME		TOTAL
MINERROR ITERATION	Cancerous	Healthy	
Number of dark pixel > Number of light pixel	20	7	28
Number of dark pixel <= Number of light pixel	15	6	20
TOTAL	35	13	

Table 4.13. Results of classifier with moments threshold and actual outcome.

	OUTCOME		TOTAL
MOMENTS	Cancerous	Healthy	
Number of dark pixel > Number of light pixel	12	3	15
Number of dark pixel <= Number of light pixel	23	10	33
TOTAL	35	13	

Table 4.14. Results of classifier with ptile threshold and actual outcome.

	OUTCOME		TOTAL
PTILE	Cancerous	Healthy	
Number of dark pixel > Number of light pixel	35	13	48
Number of dark pixel <= Number of light pixel	0	0	0
TOTAL	35	13	

Table 4.15. Results of classifier with minimum threshold and actual outcome.

	OUTCOME		TOTAL
MINIMUM	Cancerous	Healthy	
Number of dark pixel > Number of light pixel	19	7	26
Number of dark pixel <= Number of light pixel	16	6	24
TOTAL	35	13	

Whole values belong to each method are shown in Table 4.16. Highest accuracy belongs to entropy method with 91.67%. Besides, entropy gives highest specificity with 0.923 which means its chance to give negative result for healthy patient is 0.923 out of 1. Moreover, its sensitivity is 0.914 which means its chance to give positive result for cancer patient is 0.914 out of 1.

Table 4.16. Analysis results of all threshold methods.

METHOD	Sensitivity	Specificity	Positive Likelihood Ratio	Negative Likelihood Ratio	Positive Predictive Value	Negative Predictive Value	Accuracy(%)
Ideal Case	1	1	undefined	0	1	1	100
Entropy	**0.91**	**0.92**	**11.89**	**0.09**	**0.97**	**0.80**	**91.67**
Minerror	1.00	0.54	undefined	0	0.85	1.00	87.50
Ptile	1.00	0	undefined	undefined	0.73	undefined	72.92
Intermeans Iteration	0.57	0.54	1.24	0.80	0.77	0.32	56.25
Maxlike	0.54	0.46	1.01	0.99	0.73	0.27	52.08
Mean	0.54	0.54	1.18	0.85	0.76	0.30	54.17
Minerror Iteration	0.57	0.46	1.06	0.93	0.74	0.29	54.17
Minimum	0.543	0.462	1.01	0.99	0.73	0.27	52.08
Moments	0.34	0.77	1.49	0.85	0.80	0.30	45.83
Intermeans	0.31	0.69	1.02	0.99	0.73	0.27	41.67
Concavity	0.40	0.54	0.87	1.11	0.70	0.25	43.75
Intermodes	0.37	0.46	0.69	1.36	0.65	0.21	39.58
Median	0.00	1.00	undefined	undefined	undefined	0.27	27.08

Receiver Operating Characteristic (ROC) curve is a plot which displays the performance and accuracy of a diagnostic test. It shows sensitivity on the y axis and 1-specificity on the x axis for different threshold values. Diagonal line starts at point (0,0) and ends at point(1,1). It represents no predictive value. Gold standard line for ROC curve connects (0,0), (0,1) and (1,1) points, respectively. Typical ROC curve exists between these two lines.

In this thesis, percentages of the number of the light and dark pixels are calculated, firstly.

$$n_{dark} = \frac{number \quad of \quad dark \quad pixels}{total \quad number \quad of \quad pixels} \tag{4.31}$$

$$n_{light} = \frac{number \quad oflight \quad pixels}{total \quad number \quad of \quad pixels} \tag{4.32}$$

Then, difference is taken as $n_{dark} - n_{light}$. The difference is compared with varying threshold values between -1 to 1. It is bigger than threshold if input is a cancer image and it is less than threshold if input is a healthy image. Sensitivity and 1- specificity is calculated corresponds to each threshold and ROC curves are plotted. This procedure is performed for each type of histogram threshold method. ROC curves belong to each method is plotted shown in Figure 4.14.

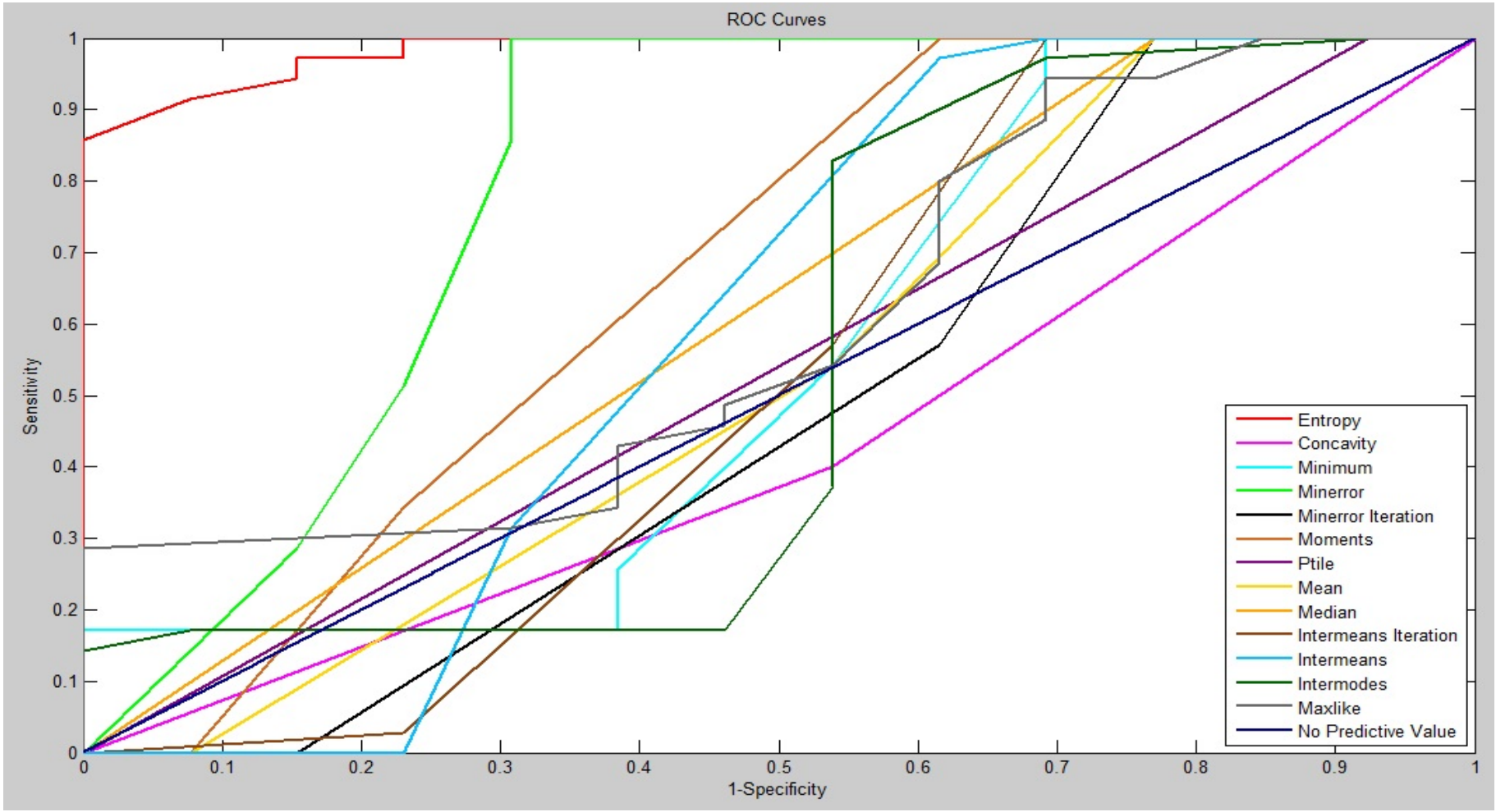

Figure 4.14. ROC Curves.

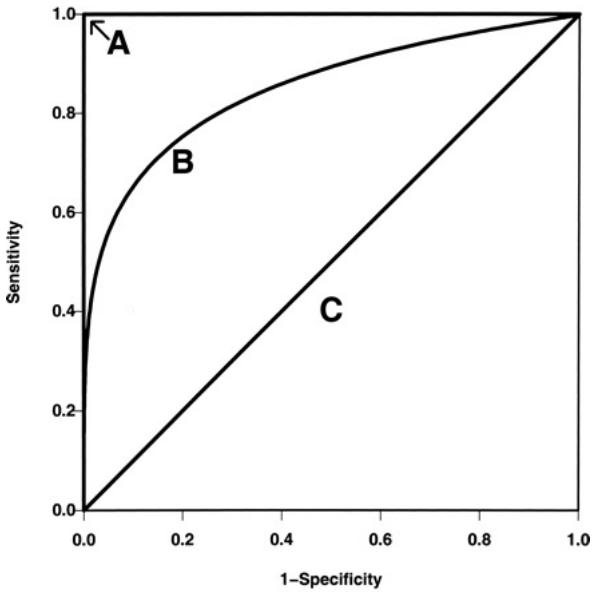

Figure 4.15. Three Hypothetical ROC Curves Representing the Diagnostic Accuracy of the Gold Standard [76].

Area under ROC curve (AUROC) is a quantitative measure shows the diagnostic accuracy. AUROC is equal to 1 if the test is perfect. Typically, AUROC is between 0.5 and 1. In Figure 4.15, A shows gold standard curve with AUROC=1, B shows a typical ROC curve AUROC=0.85 and C shows the diagonal line with AUROC=0.5. In this thesis, AUROC is calculated by using trapezoidal numerical integration. Trapezoidal method first divides area under curve into trapezoids and then estimates the total area.

Table 4.17. AUROC of all threshold methods.

	AUROC		**AUROC**
ENTROPY	0.9835	**INTERMODES**	0.5418
MINERROR	0.7978	**PTILE**	0.5385
MOMENTS	0.6692	**MEAN**	0.5341
MEDIAN	0.6154	**INTERMEANS ITERATION**	0.5242
MAXLIKE	0.6044	**MINERROR ITERATION**	0.4835
INTERMEANS	0.5934	**CONCAVITY**	0.4308
MINIMUM	0.5495		

AUROC for each histogram threshold method can be seen in Table 4.17. According to Table 4.17, entropy method has the highest AUROC. On the other hand, AUROC of concavity and minerror iteration are less than 0.5. AUROC is 0.5 if the test has no predictive value [76]. Besides, AUROC is 1 if the test is perfect. Hence, it can be deduced that concavity and minerror iteration do not offer good performance. On the contrary, entropy method offers reliable results.

Table 4.18. Entropy method AUROC with noisy image inputs.

	AUROC
Salt & Pepper (Noise Density = 0.1)	0.9319
Salt & Pepper (Noise Density = 0.2)	0.9308
Speckle (Noise Variance = 0.1)	0.9714
Speckle (Noise Variance = 0.2)	0.8945

It is observed that entropy method has the highest accuracy. Therefore, noise is added to input images and then ROC curves are plotted corresponds to entropy method shown in Figure 4.16. After plotting ROC curves, AUROC for each curve is calculated. As it can be seen in Table 4.18, if noise density or noise variance increase, AUROC decreases. In other words, noise affects test performance negatively.

In conclusion, it is observed that entropy is the most reliable histogram threshold method for cancer detection. It can be recognized from Table 4.16, 4.17 and Figure 4.14. It is thought that the reason is the non-uniform density structure of the cancerous cell. Since entropy is a measurement of the disorder, it fits perfectly for the classification.

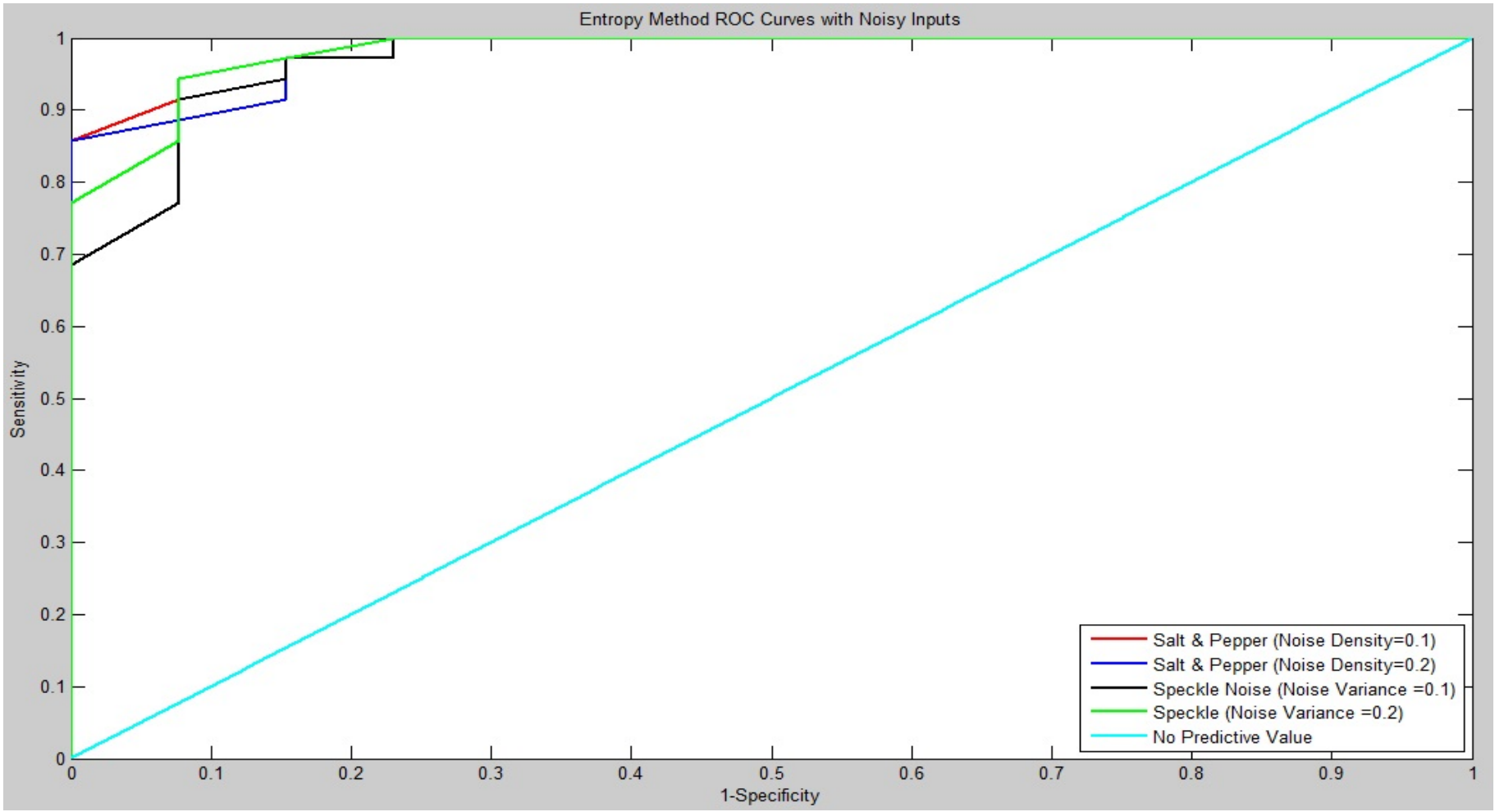

Figure 4.16. Entropy ROC Curves with Noisy Inputs.

5. CONCLUSION

This thesis is part of a novel LSCM-based cancer imaging project, which proposes several innovative approaches in designing the classifiers that are used. The proposed classifiers have subjective architectures and they can be applied in detection of any cancer type, which is uncommon in the literature. The thesis focuses on three main problems. The first problem is construction of image for LSCM. The second problem is stitching the acquired images. The last problem is cancer detection.

First of all, a circuit is designed for image construction since PMT used in the project creates current signal but DAQ card accepts only voltage signal. The circuit is developed to achieve current to voltage conversion. Secondly, an algorithm is proposed so as to transform voltage signal to a meaningful image by the help of MATLAB. Each voltage signal magnitude represents a pixel value. Besides, the algorithm performs the necessary regulation to visualize the image properly.

Secondly, acquired images are stitched. In the project explained at the introduction, images reach to computer partially and possibly rotated. It is inevitable to align and combine those images correctly. At this point an algorithm is proposed by [37] is used. Because, it is very accurate and highly suggested [38–40]. Moreover, image similarity methods are used to analyze performance of the algorithm. 11 different type of image similarity criterion are evaluated. Algorithms of some of them are improved. However, algorithms of the others are directly used since they are already improved by authors [55–57]. In order to comment about performance, an image was first seperated into three images and then stitched by the algorithm. Image similarity between original and stitched images is measured. Performance results can be found in Table 3.1. Besides, both noise and perspective effects on performance are analysed. Input images are rotated and then they are stitched. Image similarity results can be seen in Table 3.2. Additionally, noise is added to input images and then they are stitched. Image similarity results can be seen in Table 3.3. As future work, more type of image similarity criterion can be analysed. A new algorithm maybe faster and more efficient

can be implemented.

The final focus of this thesis is about cancer detection. Even though there are many studies about this topic, new approaches are presented. Two different techniques are offered. First technique is calculating RMSE value of line plot of center row of images. It is observed that generally, RMSE value of cancer images are higher than RMSE value of healthy images. Accuracy is calculated to analyse the performance. Second technique is separating image histogram into two different classes. To achieve this, finding a threshold is essential. Therefore, 13 different type of histogram thresholding methods are assessed. Algorithms of them are developed with MATLAB. To measure the performance sensitivity, specificity, positive likelihood ratio, positive predictive value, negative likelihood ratio, negative predictive value and accuracy are calculated. Results can be found in Table 4.16. Besides, ROC curves are plotted. They are shown in Figure 4.14. Moreover, AUROC is calculated for each ROC curve. Results can be seen in Table 4.17. It is understood that entropy based threshold gives the best results. In order to analyse noise effect on performance of entropy method, ROC curves are plotted with different type of noise added input images. ROC curves are shown in Figure 4.16. Finally, AUROC is calculated for each ROC curve in Figure 4.16. Results can be seen in Table 4.18. As future work, more different histogram thresholding methods can be proposed. In addition, more input images can be used.

REFERENCES

1. Siegel, R., D. Naishadham and A. Jemal, "Cancer Statistics, 2013", *CA: A Cancer Journal for Clinicians*, Vol. 63, No. 1, pp. 11–30, 2013.

2. World Health Organization and Others, *Top 10 Causes of Death (Fact sheet No. 310)*, 2007, `http://www.who.int/mediacentre/factsheets/fs310.pdf`, May 2014.

3. Goetz, T., *Why Early Detection Is the Best Way to Beat Cancer*, 2008, `http://archive.wired.com/medtech/health/magazine/17-01/ff_cancer?currentPage=all`, June 2014.

4. Ponraj, D. N., M. E. Jenifer, P. Poongodi and J. S. Manoharan, "A Survey on the Preprocessing Techniques of Mammogram for the Detection of Breast Cancer", *Journal of Emerging Trends in Computing and Information Sciences*, Vol. 2, No. 12, pp. 656–664, 2011.

5. Mahanta, L. B., D. C. Nath and C. K. Nath, "Cervix Cancer Diagnosis from Pap Smear Images Using Structure Based Segmentation and Shape Analysis", *Journal of Emerging Trends in Computing and Information Sciences*, Vol. 3, No. 2, pp. 312–325, 2012.

6. Gökdel, Y. D., *Design and Fabrication of a Biopsy Catheter Capable of Doing In-vivo Cell Imaging for Early Cancer Detection*, Tech. rep., TÜBİTAK, 2013.

7. McKinnell, R. G., R. E. Parchment, A. O. Perantoni, G. B. Pierce and I. Damjanov, *The Biological Basis of Cancer*, Cambridge University Press, Cambridge, United Kingdom, 2006.

8. Einstein, A. J., "Medical Imaging: The Radiation Issue", *Nature Reviews Cardiology*, Vol. 6, No. 6, pp. 436–438, 2009.

9. Lundstedt, C., H. Stridbeck, R. Andersson, K.-G. Tranberg and Å. Andrén-Sandberg, "Tumor Seeding Occurring After Fine-needle Biopsy of Abdominal Malignancies", *Acta Radiologica*, Vol. 32, No. 6, pp. 518–520, 1991.

10. Kumar, K., R. Avritscher, Y. Wang, N. Lane, D. C. Madoff, T.-K. Yu, J. W. Uhr and X. Zhang, "Handheld Histology-equivalent Sectioning Laser-scanning Confocal Optical Microscope for Interventional Imaging", *Biomedical Microdevices*, Vol. 12, No. 2, pp. 223–233, 2010.

11. Wilson, T., *Confocal Microscopy*, Academic Press, San Diego, CA, USA, 1990.

12. Dickensheets, D. and G. Kino, "Micromachined Scanning Confocal Optical Microscope", *Optics Letters*, Vol. 21, No. 10, pp. 764–766, 1996.

13. Silverman, S., *Oral Cancer*, People's Medical Publishing House - USA, Shelton, CT, USA, 2003.

14. Eversole, L. R., *Clinical Outline of Oral Pathology: Diagnosis and Treatment*, People's Medical Publishing House - USA, Shelton, CT, USA, 2001.

15. Sargeran, K., H. Murtomaa, S. M. R. Safavi, M. M. Vehkalahti and O. Teronen, "Survival After Diagnosis of Cancer of the Oral Cavity", *British Journal of Oral and Maxillofacial Surgery*, Vol. 46, No. 3, pp. 187–191, 2008.

16. Inoué, S., "Foundations of Confocal Scanned Imaging in Light Microscopy", *Handbook of Biological Confocal Microscopy*, pp. 1–19, Springer, Massachusetts, NY, USA, 2006.

17. Wang, Y., M. Raj, H. S. McGuff, G. Bhave, B. Yang, T. Shen and X. Zhang, "Portable Oral Cancer Detection Using a Miniature Confocal Imaging Probe with a Large Field of View", *Journal of Micromechanics and Microengineering*, Vol. 22, No. 6, p. 065001, 2012.

18. Wang, Y., S. Bish, J. W. Tunnell and X. Zhang, "MEMS Scanner Enabled Real-time Depth Sensitive Hyperspectral Imaging of Biological Tissue", *Optics Express*, Vol. 18, No. 23, pp. 24101–24108, 2010.

19. Ra, H., W. Piyawattanametha, Y. Taguchi, S. Lee, M. J. Mandella and O. Solgaard, "Two-dimensional MEMS Scanner for Dual-axes Confocal Microscopy", *Microelectromechanical Systems, Journal of*, Vol. 16, No. 4, pp. 969–976, 2007.

20. Wang, Y., K. Kumar, L. Wang and X. Zhang, "Monolithic Integration of Binary-phase Fresnel Zone Plate Objectives on 2-axis Scanning Micromirrors for Compact Microscopes", *Optics Express*, Vol. 20, No. 6, pp. 6657–6668, 2012.

21. Gokdel, Y., B. Sarioglu, S. Mutlu and A. Yalcinkaya, "Design and Fabrication of Two-axis Micromachined Steel Scanners", *Journal of Micromechanics and Microengineering*, Vol. 19, No. 7, p. 075001, 2009.

22. Liu, J. T., N. O. Loewke, H. Ra, O. Solgaard, C. H. Contag, G. S. Kino, W. Piyawattanametha, H. Haeberle and M. J. Mandella, "Micromirror-scanned Dual-axis Confocal Microscope Utilizing a Gradient-index Relay Lens for Image Guidance During Brain Surgery", *Journal of Biomedical Optics*, Vol. 15, No. 2, pp. 026029–026029, 2010.

23. Baran, U., D. Brown, S. Holmstrom, D. Balma, W. O. Davis, P. Muralt and H. Urey, "Resonant PZT MEMS Scanner for High-resolution Displays", *Microelectromechanical Systems, Journal of*, Vol. 21, No. 6, pp. 1303–1310, 2012.

24. Liu, C., *Foundations of MEMS*, Prentice Hall, Upper Saddle River, NJ, USA, 2006.

25. Kumar, K. and X. J. Zhang, "CMOS-Compatible 2-Axis Self-Aligned Vertical Comb-Driven Micromirror for Large Field-of-View Microendoscopes", *International Conference on Micro Electro Mechanical Systems, 2009. MEMS 2009. IEEE 22nd*, pp. 1015–1018, 2009.

26. Wang, Y., Y. Gokdel, N. Triesault, C. Spruell, A. Hu, D. Waters and X. Zhang, "Magnetic-actuated Stainless Steel Micro-scanner for Confocal Hyperspectral Fluorescence Microscope", *Optical MEMS and Nanophotonics,2012. OMN 2012.*, pp. 37–38, IEEE, 2012.

27. Kimoto, S., R. Omoto, M. Tsunemoto, T. Muroi, K. Atsumi and R. Uchida, "Ultrasonic Tomography of the Liver and Detection of Heart Atrial Septal Defect with the Aid of Ultrasonic Intravenous Probes", *Ultrasonics*, Vol. 2, No. 2, pp. 82–86, 1964.

28. Kossoff, G., "Diagnostic Applications of Ultrasound in Cardiology", *Australasian Radiology*, Vol. 10, No. 2, pp. 101–106, 1966.

29. Eggleton, R., C. Townsend, G. Kossoff, J. Herrick, R. Hunt, G. Templeton and J. Mitchell, "Computerised Ultrasonic Visualization of Dynamic Ventricular Configurations", *-International Conference on Medical and Biological Engineering, 2014. ICMBE 8th*, pp. 10–3, 1969.

30. Lima, E., T. Henriques-Coelho, C. Rolanda, J. M. Peˆgo, D. Silva, J. L. Carvalho and J. Correia-Pinto, "Transvesical Thoracoscopy: A Natural Orifice Translumenal Endoscopic Approach for Thoracic Surgery", *Surgical Endoscopy*, Vol. 21, No. 6, pp. 854–858, 2007.

31. De Palma, G., S. Siciliano, P. Addeo, F. Salvatori, M. Persico, S. Masone, M. Rega, F. Maione, B. E. Coppola, E. Serrao *et al.*, "A Notes Approach for Thoracic Surgery: Transgastric Thoracoscopy via a Diaphragmatic Incision in a Survival Porcine Model", *Minerva Chirurgica*, Vol. 65, No. 1, pp. 11–15, 2010.

32. Wikipedia, *Data Acquisition*, 2014, `http://en.wikipedia.org/w/index.php?title=Data_acquisition&oldid=607129252`, June 2014.

33. Wikipedia, *Photomultiplier*, 2014, `http://en.wikipedia.org/w/index.php?title=Photomultiplier&oldid=612740430`, June 2014.

34. Flyckt, S. and C. Marmonier, *Photomultiplier Tubes: Principles and Applications*, Tech. rep., Photonis, 2002.

35. Kume, H., *Photomultiplier Tube: Principle to Application*, Hamamatsu Photonics, Japan, 1994.

36. Brown, M. and D. Lowe, "Recognising Panoramas", *International Conference on Computer Vision, 2003. ICCV 2003. IEEE 9th*, Vol. 2, pp. 1218–1225, 2003.

37. Vu, P. H., *Image Stitching in Matlab*, 2013, `http://phvu.net/2013/04/10/image-stitch-matlab/`, Dec 2013.

38. Mikolajczyk, K. and C. Schmid, "A Performance Evaluation of Local Descriptors", *IEEE Transactions on Pattern Analysis and Machine Intelligence*, Vol. 27, No. 10, pp. 1615–1630, 2005.

39. Lacey, A., N. Pinitkarn and N. A. Thacker, "An Evaluation of the Performance of RANSAC Algorithms for Stereo Camera Calibrarion", *British Machine Vision Conference*, pp. 1–10, 2000.

40. Raguram, R., J.-M. Frahm and M. Pollefeys, "A Comparative Analysis of RANSAC Techniques Leading to Adaptive Real-time Random Sample Consensus", *European Conference on Computer Vision. ECCV 2008.*, pp. 500–513, Springer, 2008.

41. Lowe, D. G., "Distinctive Image Features from Scale-invariant Keypoints", *International Journal of Computer Vision*, Vol. 60, No. 2, pp. 91–110, 2004.

42. Lindeberg, T., *Scale Invariant Feature Transform*, 2012, `http://www.scholarpedia.org/article/Scale_Invariant_Feature_Transform`, May 2014.

43. Pani, A., P. Shende, M. Dhumal, K. Sangle and S. Shiravale, "Advantages of Using SIFT for Brain Tumor Detection", *International Journal of Students Research in*

Technology and Management, Vol. 1, No. 3, pp. 327–338, 2013.

44. Wu, J., Z. Cui, V. S. Sheng, P. Zhao, D. Su and S. Gong, "A Comparative Study of SIFT and Its Variants", *Measurement Science Review*, Vol. 13, No. 3, pp. 122–131, 2013.

45. Fischler, M. A. and R. C. Bolles, "Random Sample Consensus: A Paradigm for Model Fitting with Applications to Image Analysis and Automated Cartography", *Communications of the ACM*, Vol. 24, No. 6, pp. 381–395, 1981.

46. Ostiak, P., "Implementation of HDR Panorama Stitching Algorithm", *Proceedings of the 2006 CESCG Central European Seminar on Computer Graphics for students*, pp. 24–26, 2006.

47. Witkin, A. P., "Scale-space Filtering: A New Approach to Multi-scale Description", *International Conference on Acoustics, Speech, and Signal Processing*, Vol. 9, pp. 150–153, 1984.

48. Dubrofsky, E., *Homography Estimation*, Ph.D. Thesis, University of British Columbia, 2009.

49. Liang, B., Z. Chen and N. Pears, "Uncalibrated Two-view Metrology", *Proceedings of 2004 International Conference on Pattern Recognition*, Vol. 1, pp. 96–99, 2004.

50. Jae Lee, J. and G. Kim, "Robust Estimation of Camera Homography Using Fuzzy RANSAC", *International Conference on Computational Science and Its Applications. ICCSA 2007.*, pp. 992–1002, 2007.

51. Patil, T., S. Mishra, P. Chaudhari and S. Khandale, "Image Stitching Using Matlab", *International Journal of Engineering Trends and Technology*, Vol. 4, No. 3, pp. 302–306, 2013.

52. Derpanis, K. G., *Overview of the RANSAC Algorithm*, Tech. rep., Computer Sci-

ence, York University, 2010.

53. Pitié-Salpêtrière Hospital - The Ohio State University, *Mitosis Detection in Breast Cancer Histological Images*, 2011, `http://ipal.cnrs.fr/ICPR2012/?q=node/5`, May 2014.

54. Silva, E. A., K. Panetta and S. S. Agaian, "Quantifying Image Similarity Using Measure of Enhancement by Entropy", *Defense and Security Symposium*, pp. 65790U–65790U, International Society for Optics and Photonics, 2007.

55. Wang, Z. and A. C. Bovik, "A Universal Image Quality Index", *Signal Processing Letters, IEEE*, Vol. 9, No. 3, pp. 81–84, 2002.

56. Wang, Z., A. C. Bovik, H. R. Sheikh and E. P. Simoncelli, "Image Quality Assessment: From Error Visibility to Structural Similarity", *IEEE Transactions on Image Processing*, Vol. 13, No. 4, pp. 600–612, 2004.

57. Zhang, L., D. Zhang and X. Mou, "FSIM: A Feature Similarity Index for Image Quality Assessment", *IEEE Transactions on Image Processing*, Vol. 20, No. 8, pp. 2378–2386, 2011.

58. Owens, R., *Histogram Equalization*, 1997, `http://homepages.inf.ed.ac.uk/rbf/CVonline/LOCAL_COPIES/OWENS/LECT5/node3.html`, May 2014.

59. Otsu, N., "A Threshold Selection Method from Gray-level Histograms", *Automatica*, Vol. 11, No. 285-296, pp. 23–27, 1975.

60. Kumar, V., D. K. Garg and R. Kumar, "Pulmonary Nodules Diagnosis from X-Ray Imaging Using Image Processing", *International Conference on Recent Trends of Computer Technology in Academia*, pp. 21–23, 2012.

61. Gopinath, N., "Extraction of Cancer Cells from MRI Prostate Image Using MATLAB", *International Journal of Engineering Science and Innovative Technology*,

Vol. 1, No. 1, pp. 27–35, 2012.

62. Fitzke, F., B. Masters, R. Buckley and L. Speedwell, "Fourier Transform Analysis of Human Corneal Endothelial Specular Photomicrographs", *Experimental Eye Research*, Vol. 65, No. 2, pp. 205–214, 1997.

63. Lubawy, C. and M. Skala, *Algorithm for Morphological Cancer Detection*, 2004, `http://homepages.cae.wisc.edu/~ece533/project/f04/lubawy_skala.pdf`, Dec 2013.

64. Li, Z., S. Shin, S. I. Jeon, S. H. Son and J. K. Pack, "A New Histogram-based Breast Cancer Image Classifier Using Gaussian Mixture Model", *Proceedings of the 2012 ACM Research in Applied Computation Symposium*, pp. 143–147, 2012.

65. Chapelle, O., P. Haffner and V. N. Vapnik, "Support Vector Machines for Histogram-based Image Classification", *IEEE Transactions on Neural Networks*, Vol. 10, No. 5, pp. 1055–1064, 1999.

66. R.Nithya and B.Santhi, "Comparative Study on Feature Extraction Method for Breast Cancer Classification", *Journal of Theoretical and Applied Information Technology*, Vol. 33, No. 12, pp. 220–226, 2012.

67. L Zhang, D. L., Y Liu, *IMP2, An Adjunct Marker in the Diagnosis and Grading of Cervical Intraepithelial Neoplasia*, 2010, `http://www.abstracts2view.com/uscap10/view.php?nu=USCAP10L_1212`, May 2014.

68. Glasbey, C. A., "An Analysis of Histogram-based Thresholding Algorithms", *CVGIP: Graphical Models and Image Processing*, Vol. 55, No. 6, pp. 532–537, 1993.

69. Koc, G. and B. Sarioglu, "Statistical Analysis of Threshold Algorithms in Image Processing Based Cancer Cell Detection", *Signal Processing and Communications Applications, 2014. SIU 2014. IEEE 22nd*, pp. 481–484, 2014.

70. Sahoo, P. K., S. Soltani and A. Wong, "A Survey of Thresholding Techniques", *Computer Vision, Graphics and Image Processing*, Vol. 41, No. 2, pp. 233–260, 1988.

71. Pietas, A., *Identification of the Tumour-associated Gene S100A14 and Analysis of Its Regulation*, Ph.D. Thesis, Humboldt-Universität zu Berlin, 2005.

72. CCR Connections, "Teaching an Old Drug New Tricks", Vol. 4, No. 2, 2010.

73. The University of Arizona, *Image Processing and Cancer Detection Histopathological Sections*, 1998, `http://www.biology.arizona.edu/math/problem_sets/cancer/page1.html`, June 2014.

74. University of Rochester Medical Center, *Breast Cancer Cells Outsmart the Immune System and Thrive*, 2011, `http://www.urmc.rochester.edu/news/story/index.cfm?id=3107`, June 2014.

75. Swindall, A. F., A. I. Londoño-Joshi, M. J. Schultz, N. Fineberg, D. J. Buchsbaum and S. L. Bellis, "ST6Gal-I Protein Expression is Upregulated in Human Epithelial Tumors and Correlates with Stem Cell Markers in Normal Tissues and Colon Cancer Cell Lines", *Cancer Research*, Vol. 73, No. 7, pp. 2368–2378, 2013.

76. Cabral, H. J., "Statistical Primer for Cardiovascular Research", *Circulation*, Vol. 117, pp. 698–701, 2008.